

FEATURE ARTICLE

Exciton Analysis in 2D Electronic Spectroscopy

Minhaeng Cho*

Department of Chemistry and Center for Multidimensional Spectroscopy, Division of Chemistry and Molecular Engineering, Korea University, Seoul 136-701, Korea

Harsha M. Vaswani, Tobias Brixner, Jens Stenger, and Graham R. Fleming*

*Department of Chemistry, University of California at Berkeley, Berkeley, California 94720 and Physical Biosciences Division, Lawrence Berkeley National Laboratory, Berkeley, California 94720**Received: February 15, 2005; In Final Form: March 30, 2005*

A theoretical description of femtosecond two-dimensional electronic spectroscopy of multichromophoric systems is presented. Applying the stationary phase approximation to the calculation of photon echo spectra and taking into account exciton relaxation processes, we obtain an analytic expression for numerical simulations of time- and frequency-resolved 2D photon echo signals. The delocalization of one-exciton states, spatial overlaps between the probability densities of different excitonic states, and their influences on both one- and two-dimensional electronic spectra are studied. The nature of the off-diagonal cross-peaks and the time evolution of both diagonal and off-diagonal peak amplitudes are discussed in detail by comparing experimentally measured and theoretically simulated 2D spectra of the natural Fenna–Matthews–Olson (FMO) photosynthetic light-harvesting complex. We find that there are two noncascading exciton energy relaxation pathways.

I. Introduction

Photosynthetic light-harvesting complexes contain between a few to about 100 chromophores—generally chlorophylls or bacteriochlorophylls and carotenoids—in individual protein complexes. The subtle interplay between interchromophore electronic interactions and environmental effects on individual chromophores lies at the heart of the exquisite effectiveness of these complexes in absorbing, transferring, and trapping solar energy. Such effects are harnessed to broaden solar coverage, induce directional and energy migration, exploit states that would ordinarily be ineffective in energy transfer, and produce systems that are extraordinarily robust with respect to structure and energetic disorder.^{1–3} Yet in systems where the distribution of site energies (diagonal disorder) may be at least as large as the magnitude of the electronic coupling, linear spectroscopy does not contain enough information to uniquely determine the electronic Hamiltonian. Even in a dimer, the single spectroscopic splitting between two excitonically coupled features in the spectrum arises from two site energies and one electronic coupling value. If a satisfactory model of multiple linear spectra, e.g., absorption, linear dichroism, circular dichroism, can be developed to reveal the energy ordering of the exciton levels, this type of spectral information is still quite insensitive to the spatial relationship of the excitonic states. Yet exciton dynamics (i.e., energy transfer) are controlled by both the energy difference and the spatial overlap of excitonic wave functions.

Multidimensional electronic spectroscopy holds great promise to provide incisive information on the three-dimensional electronic structure of multichromophoric complexes and aggre-

gates.^{4–23} When the number of chromophores in a given complex is N , there are N one-exciton states that are given by linear combinations of N monomer wave functions. Therefore, in principle the line shape of the absorption spectrum contains information on the N electronic transitions between the electronic ground and N one-exciton states. Since the N transition probabilities independently add up to produce the absorption spectrum, the spatiotemporal dynamics between different one-exciton states cannot be studied by using conventional linear spectroscopic techniques. On the other hand, nonlinear spectroscopies such as photon echo and pump–probe methods involve four field-matter interactions.^{23,24} There are approximately N^2 cross-peaks revealing the spatial overlap among one-exciton state probability densities, the coupling-induced delocalization of excitonic transition dipoles, and exciton relaxation in the one-exciton state manifold. In the language of pump–probe spectroscopy, these nonlinear transition pathways are called ground-state bleaching (GB) or stimulated emission (SE) contributions of which a typical transition pathway is $g \rightarrow e_1 \rightarrow g \rightarrow e_2 \rightarrow g$. In addition to the one-exciton state manifold, there exist $N(N - 1)/2$ two-exciton states, and they are given by linear combinations of doubly excited chromophore wave functions. The excited state absorption (EA) contributions from one- to two-exciton states can also produce cross-peaks, and their contribution is out-of-phase in comparison to the SE and GB terms that involve four transitions between the ground state and the one-exciton states. Owing to the interferences between (GB+SE) and EA, the two-dimensional spectrum becomes intrinsically asymmetric with respect to the diagonal line even in the case of no exciton migration. Only in the limiting case when the electronic couplings vanish, does the 2D spectrum become diagonally symmetric. Therefore, asymmetry in the 2D spectrum

* To whom correspondence should be addressed. E-mails: mcho@korea.ac.kr; grfleming@lbl.gov

at short times, before exciton relaxation plays a role, suggests that the electronic couplings are not negligibly small and the excitons are spatially delocalized over multiple chromophores.

Experimentally, two-dimensional optical heterodyne spectroscopy has been developed for infrared and electronic transitions.^{7,13,16,21,25–34} Recent technological advances allow us to record 2D spectra over a wide range of frequencies and hence for a variety of physical systems.^{7,35–37} Time-dependent electronic 2D spectra have been obtained for dilute chromophore solutions,^{10,14,15} a molecular aggregate,^{19,20} and for the Fenna–Matthews–Olson (FMO) photosynthetic light-harvesting protein of *Chlorobium tepidum*.²¹ To facilitate analysis of these new results, as well as provide the basis for an intuitive understanding of the 2D spectra, a tractable and readily computable theoretical description is required. In this paper we provide such a description. As a specific application, we analyze the 2D spectra of the FMO complex, revealing excitonic coupling and relaxation processes.

II. Nonlinear Response Function of a Multilevel System

A variety of nonlinear four-wave-mixing spectroscopies, including photon echo spectroscopy, can be conveniently described by using the following 3D response function:²⁴

$$R_{3D}(t_3, t_2, t_1) \equiv \left(\frac{i}{\hbar}\right)^3 \theta(t_1) \theta(t_2) \theta(t_3) \times \langle [[[\mu(t_3 + t_2 + t_1), \mu(t_2 + t_1)], \mu(t_1)], \mu(0)] \rho_0 \rangle \quad (1)$$

Here, the Heaviside step function was denoted as $\theta(t)$. The field-matter interactions are treated in a semiclassical way as $H_I(t) = -\hat{\mu} \cdot \mathbf{E}(\mathbf{r}, t)$. The time-dependence of the dipole operator is determined by the Heisenberg equation of motion. Expanding the three commutators in eq 1, we have

$$R_{3D}(t_3, t_2, t_1) = \left(\frac{i}{\hbar}\right)^3 \theta(t_1) \theta(t_2) \theta(t_3) \sum_{\alpha=1}^4 [R_{\alpha}(t_3, t_2, t_1) - R_{\alpha}^*(t_3, t_2, t_1)] \quad (2)$$

where the four components are

$$\begin{aligned} R_1(t_3, t_2, t_1) &\equiv \langle \mu(t_1) \mu(t_1 + t_2) \mu(t_1 + t_2 + t_3) \mu(0) \rho_0 \rangle \\ R_2(t_3, t_2, t_1) &\equiv \langle \mu(0) \mu(t_1 + t_2) \mu(t_1 + t_2 + t_3) \mu(t_1) \rho_0 \rangle \\ R_3(t_3, t_2, t_1) &\equiv \langle \mu(0) \mu(t_1) \mu(t_1 + t_2 + t_3) \mu(t_1 + t_2) \rho_0 \rangle \\ R_4(t_3, t_2, t_1) &\equiv \langle \mu(t_1 + t_2 + t_3) \mu(t_1 + t_2) \mu(t_1) \mu(0) \rho_0 \rangle \end{aligned} \quad (3)$$

The initial equilibrium density operator is denoted as ρ_0 .

The four-wave-mixing polarization is written as a triple convolution integral as

$$\mathbf{P}_{3D}(\mathbf{r}, t) = N \int_0^\infty dt_3 \int_0^\infty dt_2 \int_0^\infty dt_1 R_{3D}(t_3, t_2, t_1) \times \mathbf{E}(\mathbf{r}, t - t_3) \mathbf{E}(\mathbf{r}, t - t_3 - t_2) \times \mathbf{E}(\mathbf{r}, t - t_3 - t_2 - t_1) \quad (4)$$

where N is the number of chromophores.

For a general multilevel system, the four nonlinear response functions were shown to be expressed in terms of various linear correlation functions of fluctuating transition frequencies among different quantum states.^{4,23,24} By choosing $H_a + H_{\text{bath}}$ to be the reference Hamiltonian, the difference energy operator $V_{ba}(\tau)$ is given as

$$V_{ba}(\tau) = e^{iH_a\tau} V_{ba} e^{-iH_a\tau} = e^{iH_a\tau} (H_b - H_a) e^{-iH_a\tau} \quad (5)$$

Here, H_a and H_b are the Hamiltonians of the ground and first excited electronic states, respectively. Defining the fluctuating part of the difference energy operator as

$$\delta H_{ba}(\tau) \equiv e^{iH_a\tau} (H_b - H_a - \langle H_b - H_a \rangle_a) e^{-iH_a\tau} \quad (6)$$

and the average energy gap as $\hbar\bar{\omega}_{ba} = \langle H_b - H_a \rangle_a$, we have

$$V_{ba}(\tau) = \hbar\bar{\omega}_{ba} + \delta H_{ba}(\tau) \quad (7)$$

The four nonlinear response function components in eq 3 can be written, in terms of one-sided quantum correlation functions of $\delta H_{xy}(t)$,²³

$$\begin{aligned} R_1(t_3, t_2, t_1) &= \sum_{abcd} P(a) \mu_{ad} \mu_{dc} \mu_{cb} \mu_{ba} \exp\{i\bar{\omega}_{cb}t_3 + i\bar{\omega}_{db}t_2 \\ &\quad - i\bar{\omega}_{ba}t_1 + F_{abcd}^{(1)}(t_1, t_2, t_3)\} \\ R_2(t_3, t_2, t_1) &= \sum_{abcd} P(a) \mu_{ad} \mu_{da} \mu_{cb} \mu_{ba} \exp\{i\bar{\omega}_{cb}t_3 + i\bar{\omega}_{db}t_2 \\ &\quad + i\bar{\omega}_{da}t_1 + F_{abcd}^{(2)}(t_1, t_2, t_3)\} \\ R_3(t_3, t_2, t_1) &= \sum_{abcd} P(a) \mu_{ad} \mu_{da} \mu_{cb} \mu_{ba} \exp\{i\bar{\omega}_{cb}t_3 + i\bar{\omega}_{ca}t_2 \\ &\quad + i\bar{\omega}_{da}t_1 + F_{abcd}^{(3)}(t_1, t_2, t_3)\} \\ R_4(t_3, t_2, t_1) &= \sum_{abcd} P(a) \mu_{ad} \mu_{da} \mu_{cb} \mu_{ba} \exp\{-i\bar{\omega}_{da}t_3 - i\bar{\omega}_{ca}t_2 \\ &\quad - i\bar{\omega}_{ba}t_1 + F_{abcd}^{(4)}(t_1, t_2, t_3)\} \end{aligned} \quad (8)$$

where the four auxiliary functions, $F_{abcd}^{(j)}(t_1, t_2, t_3)$ for $j = 1 \dots 4$, are given in Supporting Information 1S. The Boltzmann factor of the ground state, $|a\rangle$, was denoted as $P(a)$, $P(a) = \exp(-E_a/k_B T)/\text{Tr}[\exp(-H/k_B T)]$. The transition dipole matrix element between $|b\rangle$ and $|a\rangle$ was denoted as $\mu_{ba} \equiv \langle b|\mu|a\rangle$.

III. Stationary Phase Approximation

Although the general expressions of the nonlinear response functions were given in eq 8, they are rather complex and useful insights can be obtained by taking the short time expansion of the response function with respect to the t_1 and t_3 time arguments. Noting that the system is in highly oscillating coherence states during the first and third time periods and that the four-wave-mixing polarization is given by triple integrations over t_1 , t_2 , and t_3 , only the short time (slowly varying) parts of the molecular response during t_1 and t_3 are important and are sufficient to approximately describe the quantum decoherence processes.^{4,5,38–41} In the case of photon echo spectroscopy, during the second time period, t_2 , the system is in either a vibrational coherence state or a population state in either the electronic ground or excited state.^{23,42} Consequently, both spectral diffusion and the correlation between the excitation and probing frequencies should be properly taken into account. One can achieve this goal by taking a two-dimensional Taylor expansion of $F_{abcd}^{(j)}(t_1, t_2, t_3)$ with respect to t_1 and t_3 as

$$\begin{aligned} F_{abcd}^{(j)}(t_1, t_2, t_3) &= f_j(t_2) - \frac{1}{2} \delta_j^2(t_2) t_1^2 - \frac{1}{2} \Delta_j^2(t_2) t_3^2 + H_j(t_2) t_1 t_3 \\ &\quad + iQ_j(t_2) t_3 \end{aligned} \quad (9)$$

where the expansion coefficients $f_j(t_2)$, $\delta_j^2(t_2)$, $\Delta_j^2(t_2)$, $H_j(t_2)$, and $Q_j(t_2)$ for $j = 1 \dots 4$ are given in Supporting Information 2S and

they all are determined by the frequency–frequency correlation functions

$$\xi_{xy}(\tau_1, \tau_2) \equiv \frac{1}{\hbar^2} \langle \delta H_{xa}(\tau_1) \delta H_{ya}(\tau_2) \rangle \quad (10)$$

and $\delta H_{xa}(\tau) \equiv e^{iH_a\tau}(H_x - H_a - \langle H_x - H_a \rangle_a) e^{-iH_a\tau}$. Although the expressions for the Taylor expansion coefficients for $F_{abcd}^{(j)}(t_1, t_2, t_3)$ in Supporting Information 2S are found to be complicated, the physical meaning of each term in eq 9 can be understood as follows. The zero-order term, $f_j(t_2)$, describes the dephasing of the electronic (or vibrational) quantum beats during t_2 . The expansion coefficient, $\delta_j^2(t_2)$, corresponds to the mean square fluctuation amplitude of the transition frequency associated with the off-diagonal density matrix evolution during the first time period, t_1 , and it determines the spectral bandwidth of the corresponding 2D spectrum along the ω_τ axis where ω_τ is the conjugate Fourier frequency of t_1 in the impulsive limit. Similarly, $\Delta_j^2(t_2)$ corresponds to the mean square frequency fluctuation amplitude of the second electronic coherence state during the third time period, t_3 . The fourth term, $H_j(t_2)$, describes how the two electronic transitions separated by t_2 are correlated with each other. In the limit when $H_j(t_2) = 0$, the electronic transition induced by the first field-matter interaction is completely independent of that induced by the third field-matter interaction. As shown by Cho et al.,³⁸ the photon echo peak shift (PEPS) is directly proportional to the time evolution of $H_j(t_2)$. If the molecular system has an intrinsically static inhomogeneity, $H_j(t_2)$ does not decay to zero but to a finite value determined by the spectral width of the inhomogeneous distribution. Recently, it was theoretically shown that the slanted nature of various 2D vibrational or electronic spectra at short time ($t_2 < \text{bath correlation time}$) is also related to the transition frequency correlation term, $H_j(t_2)$.⁴¹ The last term in eq 9, $Q_j(t_2)$, describes the spectral diffusion or fluorescence Stokes shift during the second time period, t_2 . In summary, $\delta_j^2(t_2)$ is the mean square fluctuation amplitude of transition frequency during t_1 ; $\Delta_j^2(t_2)$ is the mean square fluctuation amplitude of transition frequency during t_3 ; $H_j(t_2)$ is the extent of correlation between transition frequencies during t_1 and t_3 ; and $Q_j(t_2)$ is the spectral diffusion of excited-state particles or ground-state holes during t_2 .

Two-Dimensional Photon Echo Spectroscopy. One of the most popular four-wave-mixing spectroscopies is the optical photon echo measurement.^{4–7,39,42–44} The diagrams contributing to the photon echo signal can be separated into two groups: the rephasing and nonrephasing response functions. They differ from each other by the time orderings of pulses along the incident wavevectors.

To simulate the echo spectra, we will assume that the pulse width is far shorter than any of the dynamics of interest. In this impulsive limit, the observed time-domain third-order polarization becomes linearly proportional to the associated nonlinear response function:

$$S_{\text{echo}}(t_3, t_2, t_1) \propto \text{Re}[R(t_3, t_2, t_1)] \quad (11)$$

There are various different ways to measure the photon echo polarization, depending on the experimental schemes used. In the present paper, we will consider the double Fourier transform of the photon echo response function as the reference two-dimensional photon echo spectrum, i.e.,

$$\tilde{S}_{\text{echo}}(\Omega_1, t_2, \Omega_3) \propto \int_{-\infty}^{\infty} dt_1 \int_{-\infty}^{\infty} dt_3 R(t_3, t_2, t_1) e^{\pm i\Omega_1 t_1 \pm i\Omega_3 t_3} \quad (12)$$

where Ω_j is the conjugate Fourier frequency of the experimentally controllable delay time t_j . The sign, + or –, must be properly chosen by considering the rotating wave approximation for a given experimental arrangement.

In general, it is not possible to analytically carry out the double integrations over t_1 and t_3 in eq 12, when the material response function is given as a complicated function of t_j . However, invoking the stationary phase (Laplace) approximation and taking into account the slowly varying parts of the nonlinear response function in the rotating frame with respect to the electronic transition frequencies during t_1 and t_3 periods, the above two-dimensional Fourier transform can be obtained analytically. For example, the double Fourier transform of the first response function component in eq 8 is found to be

$$\begin{aligned} \tilde{R}_1^{++}(\Omega_1, t_2, \Omega_3) &\equiv \int_{-\infty}^{\infty} dt_1 \int_{-\infty}^{\infty} dt_3 R_1(t_3, t_2, t_1) e^{i\Omega_1 t_1 + i\Omega_3 t_3} \\ &= \sum_{abcd} P(a) \mu_{ad} \mu_{dc} \mu_{cb} \mu_{ba} \int_{-\infty}^{\infty} dt_3 \int_{-\infty}^{\infty} dt_1 \exp\{i(\bar{\omega}_{cb} + \Omega_3)t_3 \\ &\quad + i\bar{\omega}_{db}t_2 - i(\bar{\omega}_{ba} - \Omega_1)t_1\} \\ &\quad \times \exp\left(f_1(t_2) - \frac{1}{2}\delta_1^2(t_2)t_1^2 - \frac{1}{2}\Delta_1^2(t_2)t_3^2\right. \\ &\quad \left.+ H_1(t_2)t_1t_3 + iQ_1(t_2)t_3\right) \\ &= \sum_{abcd} P(a) \mu_{ad} \mu_{dc} \mu_{cb} \mu_{ba} e^{i\bar{\omega}_{db}t_2 + f_1(t_2)} G\{\Omega_1 - \bar{\omega}_{ba}, \delta_1^2(t_2)\} \\ &\quad \times G\left\{\Omega_3 + \bar{\omega}_{cb} + Q_1(t_2) + \frac{H_1(t_2)(\Omega_1 - \bar{\omega}_{ba})}{\delta_1^2(t_2)},\right. \\ &\quad \left.\Delta_1^2(t_2) - \frac{H_1^2(t_2)}{\delta_1^2(t_2)}\right\} \quad (13) \end{aligned}$$

where $G\{x, y\}$ is the normalized Gaussian function defined as $G\{x, y\} = \sqrt{2\pi/y} \exp(-x^2/2y)$. The other auxiliary functions are provided in eqs 2S–a). Similarly, one can obtain expressions for the other components of the 2D spectra, $\tilde{R}_j(\Omega_3, t_2, \Omega_1)$ (for $j = 2, \dots, 4$), and their complex conjugates. Although the above expression appears to be complicated, the physical meaning of each term is rather straightforward. The first Gaussian function has a variance of $\delta_1^2(t_2)$ and its center frequency is determined by the ensemble averaged transition frequency between $|b\rangle$ and $|a\rangle$ states. After a finite delay time t_2 , the third pulse interacts with the molecular system and creates a coherence state $|c\rangle \langle b|$. During the second delay time t_2 , the system undergoes spectral diffusion determined by the time-dependent function, $Q_1(t_2)$ (see eq 2S-1). Also, due to the correlation between the transition frequency during t_1 and during t_3 , i.e., a finite memory effect, the spectral distribution and width of the 2D photon echo spectrum along the Ω_3 frequency axis, evolves with respect to t_2 . As described by the second Gaussian function in eq 13, the center frequency of this Gaussian function with respect to Ω_3 shifts in time due to the spectral diffusion, $Q_1(t_2)$, as well as the uphill or downhill evolution of the doorway wave packet, which is described by $H_1(t_2)(\Omega_1 - \bar{\omega}_{ba})/\delta_1^2(t_2)$. In the case of a simple two-level system, we showed that the wave packet evolution dynamics described by $H(t)$ is directly proportional to the solvation correlation function (see eq 14 in ref 41). Also, the width of the Gaussian function with respect to Ω_3 increases from $\Delta_1^2(0) - H_1^2(0)/\delta_1^2(0)$ to $\Delta_1^2(\infty)$; note that $H_1(t)$ is a decaying function.

IV. Exciton Hamiltonian and Correlation Functions

A. Exciton Representation. Photosynthetic systems consist of a number of chlorophylls that are electronically coupled to one another. To describe electronic and nonlinear optical properties of these photosynthetic systems, the Frenkel exciton Hamiltonian has been used extensively.^{45,46} Denoting a_m^\dagger and a_m to be the creation and annihilation operators of electronic excitation at the m th chromophore, the zero-order Hamiltonian can be written as

$$H_0 = \sum_{m=1}^N \epsilon_m a_m^\dagger a_m + \sum_{m \neq n}^N \sum_{n=1}^N J_{mn} a_m^\dagger a_n + H_{ph} \quad (14)$$

where the m th site energy, electronic coupling constant between the m th and n th chromophores, and the phonon bath Hamiltonian were denoted as ϵ_m , J_{mn} , and H_{ph} , respectively. The chromophore–phonon bath interaction and interchromophore distance and orientation fluctuations induce fluctuations of site energies and coupling constants. Thus, the electron–phonon interaction Hamiltonian is written as

$$H^{e-p} = \sum_m \sum_n q_{mn}(\mathbf{Q}) a_m^\dagger a_n \quad (15)$$

where $q_{mn}(\mathbf{Q})$ is an operator of bath coordinates, \mathbf{Q} , and it is assumed that the expectation values calculated over the bath states, $\langle q_{mn}(\mathbf{Q}) \rangle_0$, are zero (note that if $\langle q_{mn}(\mathbf{Q}) \rangle_0$ values are finite they can be included in the zeroth-order Hamiltonian). For $m \neq n$, the couplings to phonons can induce transitions between electronic excitations of different chromophores in the site representation. Here, the assumption that the $q_{mn}(\mathbf{Q})$ operator is linearly proportional to the bath coordinates is not necessary.

For any general four-wave-mixing spectroscopy, we need to consider three well-separated manifolds: the ground state, the N one-exciton states, and the $N(N-1)/2$ two-exciton states. The one- and two-exciton eigenvalues and eigenvectors can be obtained by considering the following one- and two-exciton Hamiltonian matrices, denoted as \tilde{H}_1 and \tilde{H}_2 , respectively, in the site representation:

$$\tilde{H}_1 = \begin{bmatrix} \epsilon_1 & J_{12} & \cdots & J_{1N} \\ J_{12} & \epsilon_2 & \cdots & J_{2N} \\ \vdots & \vdots & \ddots & \vdots \\ J_{1N} & J_{2N} & \cdots & \epsilon_N \end{bmatrix}, \quad (16)$$

$$\tilde{H}_2 = \begin{bmatrix} \epsilon_1 + \epsilon_2 & J_{23} & \cdots & J_{2N} & J_{13} & \cdots & 0 \\ J_{23} & \epsilon_1 + \epsilon_3 & \cdots & J_{3N} & J_{12} & \cdots & 0 \\ \vdots & \vdots & \ddots & \vdots & \vdots & \cdots & \vdots \\ J_{2N} & J_{3N} & \cdots & \epsilon_1 + \epsilon_N & 0 & \cdots & J_{1(N-1)} \\ J_{13} & J_{12} & \cdots & 0 & \epsilon_2 + \epsilon_3 & \cdots & 0 \\ \vdots & \vdots & \vdots & \vdots & \vdots & \ddots & \vdots \\ 0 & 0 & \cdots & J_{1(N-1)} & 0 & \cdots & \epsilon_{N-1} + \epsilon_N \end{bmatrix} \quad (17)$$

Note that $[\tilde{H}_2]_{jk} = J_{\alpha\gamma}$ when $[\tilde{H}_2]_{jj} = \epsilon_\alpha + \epsilon_\beta$ and $[\tilde{H}_2]_{kk} = \epsilon_\beta + \epsilon_\gamma$ and that $[\tilde{H}_2]_{jk} = 0$ when $[\tilde{H}_2]_{jj} = \epsilon_\alpha + \epsilon_\beta$ and $[\tilde{H}_2]_{kk} = \epsilon_\gamma + \epsilon_\delta$. To obtain the one- and two-exciton energies and states, the above two Hamiltonian matrices can be diagonalized by the corresponding orthogonal transformation matrices, U and V , as

$$\begin{aligned} U^{-1} \tilde{H}_1 U &= \tilde{\Omega} \\ V^{-1} \tilde{H}_2 V &= \tilde{W} \end{aligned} \quad (18)$$

where the diagonal elements of $\tilde{\Omega}$ and \tilde{W} matrices correspond to the one- and two-exciton eigenvalues. The one- and two-exciton states can be expanded as

$$\begin{aligned} |e_j\rangle &= \sum_m U_{jm}^{-1} |m\rangle \\ |f_k\rangle &= \sum_{m=1}^{N-1} \sum_{n=m+1}^N v_{mn}^{(k)} |m,n\rangle \end{aligned} \quad (19)$$

where $|m\rangle = a_m^\dagger |0\rangle$ and $|m,n\rangle = a_m^\dagger a_n^\dagger |0\rangle$. The eigenvector elements of the j th one-exciton and the k th two-exciton states were denoted as U_{jm}^{-1} and $v_{mn}^{(k)}$, respectively. The matrix elements of $v^{(k)}$ correspond to the elements of the k th row of the matrix V^{-1} . $v_{mn}^{(k)}$ is the weighting factor of the doubly excited state $a_m^\dagger a_n^\dagger |0\rangle$ in the k th two-exciton state.

Due to the chromophore–bath interactions, the site energies and coupling constants fluctuate in time, and according to eq 15 we need to consider the following two matrices where each matrix element is an operator of the bath degrees of freedom:

$$\begin{aligned} [\tilde{H}_1^{e-p}(\mathbf{Q})]_{mn} &= q_{mn}(\mathbf{Q}), \\ \tilde{H}_2^{e-p}(\mathbf{Q}) &= \begin{bmatrix} q_{11} + q_{22} & q_{23} & \cdots & q_{2N} & q_{13} & \cdots & 0 \\ J_{23} & q_{11} + q_{33} & \cdots & q_{3N} & q_{12} & \cdots & 0 \\ \vdots & \vdots & \ddots & \vdots & \vdots & \cdots & \vdots \\ q_{2N} & q_{3N} & \cdots & q_{11} + q_{NN} & 0 & \cdots & q_{1(N-1)} \\ q_{13} & q_{12} & \cdots & 0 & q_{22} + q_{33} & \cdots & 0 \\ \vdots & \vdots & \vdots & \vdots & \vdots & \ddots & \vdots \\ 0 & 0 & \cdots & q_{1(N-1)} & 0 & \cdots & q_{1(N-1)(N-1)} + q_{NN} \end{bmatrix} \end{aligned} \quad (20)$$

In the one- and two-exciton state representation, the above electron–phonon interaction Hamiltonian matrices can be transformed as

$$\begin{aligned} \tilde{\Xi}_1^{e-p}(\mathbf{Q}) &= U^{-1} \tilde{H}_1^{e-p}(\mathbf{Q}) U \\ \tilde{\Xi}_2^{e-p}(\mathbf{Q}) &= V^{-1} \tilde{H}_2^{e-p}(\mathbf{Q}) V \end{aligned} \quad (21)$$

The diagonal matrix elements, $[\tilde{\Xi}_1^{e-p}(\mathbf{Q})]_{jj}$ and $[\tilde{\Xi}_2^{e-p}(\mathbf{Q})]_{kk}$ describe the energy fluctuations induced by electron–phonon interaction of the j th one-exciton and the k th two-exciton state, respectively. The off-diagonal matrix elements of $\tilde{\Xi}_1^{e-p}(\mathbf{Q})$ and $\tilde{\Xi}_2^{e-p}(\mathbf{Q})$ will induce exciton relaxations within the one- and two-exciton manifolds, respectively.

B. Exciton State Energy Fluctuations. From the transformed one-exciton Hamiltonian, the energy of the j th one-exciton state, fluctuating due to electron–phonon interactions, can be written as

$$\Omega_j(\mathbf{Q}) = \tilde{\Omega}_{jj} + [\tilde{\Xi}_1^{e-p}(\mathbf{Q})]_{jj} = \tilde{\Omega}_{jj} + \sum_m \sum_n U_{jm}^{-1} q_{mn}(\mathbf{Q}) U_{nj} \quad (22)$$

We will assume that the fluctuation amplitudes of the coupling constants, q_{mn} (for $m \neq n$), are typically smaller than the fluctuation amplitudes of diagonal site energies, as in Prall et al.¹³

$$\langle q_{mn}^2 \rangle \gg \langle q_{np}^2 \rangle \text{ for all } m, n, \text{ and } p, \text{ and } n \neq p \quad (23)$$

Equation 22 can be simplified as

$$\Omega_j(\mathbf{Q}) \cong \tilde{\Omega}_{jj} + \sum_m U_{mj}^2 q_{mm}(\mathbf{Q}) \quad (24)$$

Note that the fluctuation of the j th one-exciton state energy, the second term in eq 24, is given by a linear combination of each site energy fluctuation term, $q_{mm}(\mathbf{Q})$, and the weighting factors are determined by the square of the corresponding eigenvector elements. By following the same procedure, the k th two-exciton state energy can be written as

$$\begin{aligned} W_k(\mathbf{Q}) &= \tilde{W}_{kk} + [\tilde{\Xi}_2^{\text{e-p}}(\mathbf{Q})]_{kk} \\ &= \tilde{W}_{kk} + \sum_m \sum_n V_{jm}^{-1} [\tilde{H}_2^{\text{e-p}}(\mathbf{Q})]_{mn} V_{nj} \\ &\cong \tilde{W}_{kk} + \sum_{m=1}^{N-1} \sum_{n=m+1}^N (v_{mn}^{(k)})^2 \{q_{mm}(\mathbf{Q}) + q_{nn}(\mathbf{Q})\} \end{aligned} \quad (25)$$

Again, the fluctuation of the two-exciton state energy, determined by the second term in eq 25, is given by a linear combination of two site energy fluctuations with weighting factors of $(v_{mn}^{(k)})^2$. Note that energy fluctuation at the m th site, described by $q_{mm}(\mathbf{Q})$, will modulate both the one- and two-exciton state energies, and the relative weights are determined by the eigenvector matrix elements. Consequently, as will be shown below, the fluctuation of the j th one-exciton transition frequency is intrinsically correlated with the fluctuation of other one- or two-exciton transition frequencies. Because of this instantaneous correlation mediated by the electronic couplings, the one- and two-color photon echo peak shifts can be used to study the spatial extent of exciton delocalization as well as the spatial overlap between different one or two-exciton state probability densities.^{17,38} We will present the results on the PEPS of a multichromophoric system elsewhere.

C. Transition Dipoles. Once the eigenvectors of the one- and two-exciton states are determined, the exciton transition dipole matrix elements can be expressed as linear combinations of site transition dipoles, i.e.,

$$\begin{aligned} \mu_{e_j} &\equiv \langle 0 | \hat{\mu} | e_j \rangle = \sum_m U_{jm}^{-1} d_m \\ \mu_{e_j f_k} &\equiv \langle e_j | \hat{\mu} | f_k \rangle = \sum_{m=1}^{N-1} \sum_{n=m+1}^N v_{mn}^{(k)} (U_{jm}^{-1} d_m + U_{jn}^{-1} d_n) \end{aligned} \quad (26)$$

where d_m is the transition dipole vector of the m th chromophore, i.e., $d_m \equiv \langle 0 | \hat{\mu} | m \rangle$. These transition dipole matrix elements in eq 26 will be used to calculate various photon echo response functions.

D. Correlation Functions of Fluctuating One- and Two-Exciton Transition Frequencies. As shown in section III, for a multilevel system such as the N -coupled chromophore system considered in the present section, we need both the autocorrelation functions and the cross-correlation functions of the one- or two-exciton transition frequencies to calculate the nonlinear response functions. Using the approximate expressions in eq 24, we find that the time-correlation between any given two one-exciton transition frequencies is

$$\langle \delta\Omega_j(t) \delta\Omega_k(0) \rangle = \sum_m \sum_n U_{mj}^2 U_{nk}^2 \langle q_{mm}(t) q_{nn}(0) \rangle \quad (27)$$

where $\delta\Omega_j(\mathbf{Q}) = \Omega_j(\mathbf{Q}) - \tilde{\Omega}_{jj}$ and $\delta\Omega_j(t) = \exp(iH_{ph}t/\hbar) \delta\Omega_j(\mathbf{Q}) \exp(-iH_{ph}t/\hbar)$. If the energy fluctuation at the m th chromophore is statistically independent of the energy fluctuation at the n th chromophore, i.e.,

$$\langle q_{mm}(t) q_{nn}(0) \rangle = \delta_{mn} \langle q_{mm}(t) q_{mm}(0) \rangle \quad (28)$$

then eq 27 simplifies to

$$\langle \delta\Omega_j(t) \delta\Omega_k(0) \rangle = \sum_m U_{mj}^2 U_{mk}^2 \langle q_{mm}(t) q_{mm}(0) \rangle \quad (29)$$

Note that the approximation, eq 28, was found to be reasonable even for a dimer system, as experimentally shown by Prall et al.¹³ We further assume that the site energy fluctuation correlation functions $\langle q_{mm}(t) q_{mm}(0) \rangle$ are all identical so that we have

$$\langle q_{mm}(t) q_{mm}(0) \rangle = C(t) \text{ (for all } m) \quad (30)$$

For the sake of later use, $C(t)$ is divided into the real and imaginary parts as

$$C(t) = a(t) + ib(t) \quad (31)$$

By introducing the spectral density representing the spectral distribution of the chromophore–bath coupling constants, the real and imaginary parts, $a(t)$ and $b(t)$, can be written as integrals over the spectral density, i.e.,

$$a(t) = \int_0^\infty d\omega \rho(\omega) \coth\left[\frac{\hbar\omega}{2k_B T}\right] \omega^2 \cos \omega t \quad (32)$$

$$b(t) = \int_0^\infty d\omega \rho(\omega) \omega^2 \sin \omega t \quad (33)$$

Note that the absolute magnitude of the spectral density is determined by the solvent reorganization energy as $\lambda = \hbar \int_0^\infty d\omega \omega \rho(\omega)$,⁴ i.e., λ is the oscillator energy averaged over the spectral density. Since the initial value of $C(t)$, which is the mean square fluctuation amplitude of the transition frequency of an isolated chromophore, is critical in the following derivations and discussions, it is especially denoted as

$$\begin{aligned} C_0 &= C(0) = \langle \omega^2 \coth[\hbar\omega/2k_B T] \rangle_\rho \\ &= \int_0^\infty d\omega \rho(\omega) \coth[\hbar\omega/2k_B T] \omega^2 \end{aligned} \quad (34)$$

By using the approximation of eq 30, eq 29 is further simplified as

$$\langle \delta\Omega_j(t) \delta\Omega_k(0) \rangle = \left(\sum_m U_{mj}^2 U_{mk}^2 \right) C(t) \quad (35)$$

We next consider the correlation functions between any given two two-exciton transition frequencies, and they are found to be

$$\begin{aligned} \langle \delta W_j(t) \delta W_k(0) \rangle &= \sum_{m=1}^{N-1} \sum_{n=m+1}^N \sum_{r=1}^{N-1} \sum_{s=r+1}^N (v_{mn}^{(j)})^2 (v_{rs}^{(k)})^2 \\ &\quad \times \langle \{q_{mm}(t) + q_{nn}(t)\} \{q_{rr}(0) + q_{ss}(0)\} \rangle \\ &\cong \left(\sum_{m=1}^{N-1} \sum_{n=m+1}^N (v_{mn}^{(j)})^2 \{P_m^{(k)} + P_n^{(k)}\} \right) C(t) \end{aligned} \quad (36)$$

where the second equality was obtained by invoking the approximation in eq 30, and

$$P_m^{(k)} \equiv \sum_{j=1}^{m-1} (v_{jm}^{(k)})^2 + \sum_{j=m+1}^N (v_{mj}^{(k)})^2 \quad (37)$$

In addition to the correlation functions between two one-exciton state frequency fluctuations and between two two-exciton state frequency fluctuations, the cross-correlation functions between $\delta\Omega_j(t)$ and $\delta W_k(0)$ are required in calculating the nonlinear response functions. They are

$$\begin{aligned} \langle \delta\Omega_j(t) \delta W_k(0) \rangle &= \sum_{m=1}^N \sum_{r=1}^{N-1} \sum_{s=r+1}^N U_{mj}^2 v_{rs}^{(k)2} \langle q_{mm}(t) \{q_{rr}(0) + q_{ss}(0)\} \rangle \\ &\equiv \left(\sum_{m=1}^N U_{mj}^2 P_m^{(k)} \right) C(t) \end{aligned} \quad (38)$$

In this subsection, invoking the two approximations, eqs 28 and 30, we showed that all auto- and cross-correlation functions of one- or two-exciton state frequency fluctuations can be written in terms of the scaled frequency-frequency correlation function of a single chromophore, $C(t)$.

E. Delocalization and Spatial Overlap of Excitons. In eqs 35, 36, and 38, three different correlation functions of one- and two-exciton state frequency fluctuations were obtained. In the present subsection, we will provide physical meaning of each term and its connection to either the spatial delocalization of the corresponding exciton or the spatial overlap between the excitonic state probability densities.

First, let us consider the mean square fluctuation amplitude of the j th one-exciton transition frequency, $\langle \delta\Omega_j^2 \rangle$. From eq 35, we find

$$\frac{\langle \delta\Omega_j^2 \rangle}{C_0} = \sum_m U_{mj}^4 = \frac{1}{N_j} \quad (39)$$

This ratio is the inverse of the “inverse participation ratio (IPR)” of the j th one-exciton state, where the IPR was defined as $N_j = [\sum_m U_{mj}^4]^{-1}$. Note that the IPR is a measure of how many molecules are involved in a given exciton, and the ratio $\langle \delta\Omega_j^2 \rangle / C_0$ will provide direct evidence of the extent of delocalization of the j th exciton. In the limit of complete localization, $\langle \delta\Omega_j^2 \rangle = C_0$ and $(\sum_m U_{mj}^4)^{-1} = 1$. On the other hand, if the j th exciton is fully delocalized with $U_{mj} = 1/\sqrt{N}$, the ratio $\langle \delta\Omega_j^2 \rangle / C_0$ becomes $1/N$ so that the mean square fluctuation amplitude of the j th exciton becomes very small (by a factor of $1/N$) in comparison to that of an isolated chromophore. This phenomenon is the well-known exchange narrowing effect—the absorption spectrum of a coupled chromophore system (for example a J -aggregate^{47–49}) is significantly narrower than that of a single chromophore in the same condensed phase.

Second, let us consider the magnitude of the cross-correlation function, $\langle \delta\Omega_j(t) \delta\Omega_k(0) \rangle$. The ratio $\langle \delta\Omega_j \delta\Omega_k \rangle / C_0$ is given by

$$\frac{\langle \delta\Omega_j \delta\Omega_k \rangle}{C_0} = \sum_m U_{mj}^2 U_{mk}^2 \quad (40)$$

Noting that the vector, $\vec{p}_j = (U_{1j}^2, U_{2j}^2, \dots)$, can be understood as a probability density distribution of the j th exciton state in the site representation, we have

$$\langle \delta\Omega_j \delta\Omega_k \rangle / C_0 = \vec{p}_j \cdot \vec{p}_k \quad (41)$$

which can be viewed as the *spatial overlap of the two probability density distributions*, \vec{p}_j and \vec{p}_k , of the j th and k th exciton states. As an example, consider a complex with five chro-

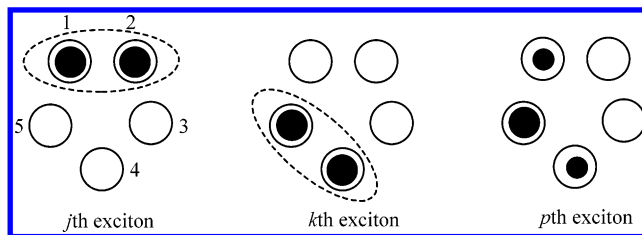


Figure 1. Spatial distribution of three excitons in a hypothetical five chromophore system. The size of the filled circle is proportional to U_{mj}^2 .

mophores (see Figure 1). Suppose that the j th exciton is delocalized over chromophores 1 and 2 and that the k th exciton is delocalized over chromophores 4 and 5, as illustrated in Figure 1. The size of the filled circle for each chromophore is proportional to U_{mj}^2 . In this case, the spatial overlap $\vec{p}_j \cdot \vec{p}_k$ is zero and consequently the amplitude of $\langle \delta\Omega_j(t) \delta\Omega_k(0) \rangle$ is negligibly small because the two exciton states do not involve any common chromophores. On the other hand, the probability density distribution of the p th exciton in Figure 1 overlaps strongly with that of the k th exciton so that $\langle \delta\Omega_k \delta\Omega_p \rangle / C_0$ is larger than $\langle \delta\Omega_j \delta\Omega_p \rangle / C_0$. Consequently, the fluctuating k th exciton transition frequency is (in-phase) correlated with the p th exciton transition frequency. Therefore, an experimental method that can selectively measure $\langle \delta\Omega_j \delta\Omega_k \rangle$, will provide spatial information about a pair of excitons that have different frequencies. We found that the two-color photon echo peak shift measurement, where the two different frequencies are simultaneously resonant with the j th and k th one-exciton states, can be used to measure this particular quantity; a detailed discussion of the two-color photon echo peak shift measurement will be presented elsewhere.

We next consider the cross-correlation between the j th one-exciton state frequency fluctuation and the k th two-exciton state frequency fluctuation, $\langle \delta\Omega_j(t) \delta W_k(0) \rangle$. Its amplitude divided by C_0 is

$$\frac{\langle \delta\Omega_j \delta W_k \rangle}{C_0} = \sum_{m=1}^N U_{mj}^2 P_m^{(k)} \quad (42)$$

To understand the physical meaning of the quantity, $\sum_{m=1}^N U_{mj}^2 P_m^{(k)}$, let us define the projection operator, $\hat{P}_m = |m\rangle \langle m|$, where $|m\rangle$ denotes the singly excited state of the m th chromophore. Then, one can prove that

$$P_m^{(k)} = \langle f_k | \hat{P}_m | f_k \rangle \quad (43)$$

where $|f_k\rangle$ is the k th two-exciton state wave function, i.e.,

$$|f_k\rangle = \sum_{m=1}^{N-1} \sum_{n=m+1}^N v_{mn}^{(k)} |m\rangle |n\rangle \quad (44)$$

Therefore, $P_m^{(k)}$ is the expectation value of \hat{P}_m over the probability distribution of the k th two-exciton state and is considered to be the “amount” of the $|m\rangle$ wave function in the k th two-exciton state. In other words, $\vec{P}_k \equiv (P_1^{(k)}, P_2^{(k)}, \dots)$ vector is the *reduced (projected) probability density* of each site in the k th two-exciton state. Therefore, eq 42 can be rewritten as

$$\frac{\langle \delta\Omega_j \delta W_k \rangle}{C_0} = \vec{p}_j \cdot \vec{P}_k \quad (45)$$

which can be interpreted as the spatial overlap between the probability density of the j th one-exciton and the reduced probability density of the k th two-exciton state.

Finally, the mean square fluctuation amplitude of the k th two-exciton state is found to be

$$\frac{\langle \delta W_k^2 \rangle}{C_0} = \sum_{m=1}^{N-1} \sum_{n=m+1}^N (v_{mn}^{(k)})^2 \{P_m^{(k)} + P_n^{(k)}\} \quad (46)$$

This result suggests that $\langle \delta \Omega_k^2 \rangle$ is determined by the overlap of the probability density of the k th two-exciton in the $|m, n\rangle$ basis and the projected (reduced) probability densities.

V. Exciton Relaxation and 2D Photon Echo

The one- and two-exciton states are linear combinations of $|m\rangle$ and $|m, n\rangle$ local states, respectively. The zero-order Hamiltonians were diagonalized to obtain the one- and two-exciton states and the diagonal elements of $\tilde{\Xi}_1^{e-p}(\mathbf{Q})$ and $\tilde{\Xi}_2^{e-p}(\mathbf{Q})$ were taken into account to quantitatively describe the fluctuations of one- and two-exciton state energies induced by the chromophore–bath (electron–phonon) interactions. However, the off-diagonal matrix elements of $\tilde{\Xi}_1^{e-p}(\mathbf{Q})$ and $\tilde{\Xi}_2^{e-p}(\mathbf{Q})$ in the exciton basis can further induce exciton relaxations in either the one- or two-exciton manifolds. In the present section, treating these off-diagonal matrix elements of $\tilde{\Xi}_1^{e-p}(\mathbf{Q})$ as perturbations and using second-order perturbation theory, we calculate the relaxation rates required in constructing a proper master equation. The relaxation rate constant for the transition from the population state of the $|e_j\rangle$ exciton to that of the $|e_k\rangle$ exciton can be obtained from the second-order Fermi Golden Rule as⁵⁰

$$K_{kj}(\Delta\Omega_{kj}) = 2\text{Re} \int_0^\infty dt \langle [\tilde{\Xi}_1^{e-p}(\mathbf{Q}(t))]_{jk} [\tilde{\Xi}_1^{e-p}(\mathbf{Q}(0))]_{kj} \rangle \times \exp\{-i\Delta\Omega_{kj}t\} \quad (47)$$

where $\Delta\Omega_{kj} = \Omega_k - \Omega_j$. Now, depending on the definition of propagation operator for the time-evolution of $[\tilde{\Xi}_1^{e-p}(\mathbf{Q}(t))]_{jk}$, one can obtain either the conventional Redfield theory rates or the modified Redfield theory rates.⁵¹ Note that the diagonal elements $[\tilde{\Xi}_1^{e-p}(\mathbf{Q})]_{jj} = [U^{-1}\tilde{H}_1^{e-p}(\mathbf{Q})U]_{jj}$ are in general dependent on the bath degrees of freedom. If one ignores these diagonal matrix elements, $[\tilde{\Xi}_1^{e-p}(\mathbf{Q})]_{jj}$, in the propagation of $[\tilde{\Xi}_1^{e-p}(\mathbf{Q}(t))]_{jk}$, we have

$$[\tilde{\Xi}_1^{e-p}(\mathbf{Q}(t))]_{jk} = \exp\{iH_{\text{ph}}t/\hbar\} [\tilde{\Xi}_1^{e-p}(\mathbf{Q})]_{jk} \exp\{-iH_{\text{ph}}t/\hbar\} \quad (48)$$

where H_{ph} is the phonon bath Hamiltonian. In this case, the trace in eq 47 is over the phonon eigenstates. On the other hand, if the diagonal elements, $[\tilde{\Xi}_1^{e-p}(\mathbf{Q})]_{jj}$, are not negligibly small, e.g., strong system-bath couplings,^{50–54} the better time evolution of $[\tilde{\Xi}_1^{e-p}(\mathbf{Q}(t))]_{jk}$ is given as

$$[\tilde{\Xi}_1^{e-p}(\mathbf{Q}(t))]_{jk} = \exp\left\{\frac{i(H_{\text{ph}} + [\tilde{\Xi}_1^{e-p}(\mathbf{Q})]_{jj})t}{\hbar}\right\} [\tilde{\Xi}_1^{e-p}(\mathbf{Q})]_{jk} \exp\left\{-\frac{i(H_{\text{ph}} + [\tilde{\Xi}_1^{e-p}(\mathbf{Q})]_{kk})t}{\hbar}\right\} \quad (49)$$

and the quantum mechanical trace in eq 47 should be performed over the eigenstates of the phonon plus $[\tilde{\Xi}_1^{e-p}(\mathbf{Q})]_{jj}$ Hamiltonians. Note that each of these is a collection of displaced harmonic oscillators. This is the case of the intermediate coupling limit studied by Mukamel and co-workers^{45,46} and Yang and Fleming.⁵¹

A. Modified Redfield Theory. Using the propagated off-diagonal Hamiltonian matrix element given in eq 49 and applying the cumulant expansion method to the calculations of the correlation function, $\langle [\tilde{\Xi}_1^{e-p}(\mathbf{Q}(t))]_{jk} [\tilde{\Xi}_1^{e-p}(\mathbf{Q}(0))]_{kj} \rangle$, one can obtain the modified Redfield rate constant,^{45,51}

$$K_{kj}(\Delta\Omega_{kj}) = 2\text{Re} \int_0^\infty dt f_{kj}(t) \exp\{-i\Delta\Omega_{kj}t\} \quad (50)$$

where

$$f_{kj}(t) = [\ddot{g}_{jk,kj}(t) - \{\dot{g}_{jk,kk}(t) - \dot{g}_{jk,jj}(t) - 2i\lambda_{jk,jj}/\hbar\} \times \{\dot{g}_{kj,kk}(t) - \dot{g}_{kj,jj}(t) - 2i\lambda_{kj,jj}/\hbar\}] \times \exp[-g_{kk,kk}(t) - g_{jj,jj}^*(t) + 2\{g_{kk,jj}(t) + i\lambda_{kk,jj}t/\hbar\}] \quad (51)$$

Here, the line shape functions, $g_{ab,cd}(t)$, and the associated solvent reorganization energies, $\lambda_{ab,cd}$, are defined as

$$g_{ab,cd}(t) = \left(\sum_m U_{am}^{-1} U_{mb} U_{cm}^{-1} U_{md}\right) \int_0^t d\tau \int_0^\tau d\tau' C(\tau') \quad (52)$$

$$\lambda_{ab,cd} = \left(\sum_m U_{am}^{-1} U_{mb} U_{cm}^{-1} U_{md}\right) \lambda$$

B. Master Equation. Once the rate constants are all determined, one can obtain the conditional probability, $G_{kj}(t)$, of finding state $|k\rangle$ at time t given that it was at state $|j\rangle$ at $t = 0$ by solving the master equation

$$\dot{G}_{kj}(t) = \sum_{l \neq k} K_{kl} G_{lj}(t) - \left(\sum_{l \neq k} K_{lk}\right) G_{kj}(t) \quad (53)$$

with the initial conditions, $G_{kj}(0) = \delta_{kj}$. These coupled linear differential equations can be solved by using the Laplace transform method. Denoting the Laplace transform of $G_{kj}(t)$ as $\tilde{G}_{kj}(s)$, one can rewrite the above initial value problem as

$$s\tilde{\underline{G}}(s) + \underline{\underline{K}}\tilde{\underline{G}}(s) = \underline{\underline{I}} \quad (54)$$

where the underlined terms in the above equation denote an N by N matrix, and $\underline{\underline{I}}$ is the identity matrix. The $[j,k]$ th matrix element of $\tilde{\underline{G}}(s)$ is $\tilde{G}_{jk}(s)$. The rate constant matrix $\underline{\underline{K}}$ is defined as

$$\underline{\underline{K}} = \begin{pmatrix} \sum_{j \neq 1}^N K_{j1} & -K_{12} & \cdots & -K_{1N} \\ -K_{21} & \sum_{j \neq 2}^N K_{j2} & & -K_{2N} \\ & & \ddots & \\ -K_{N1} & -K_{N2} & \cdots & \sum_{j \neq N}^N K_{jN} \end{pmatrix} \quad (55)$$

where the rate constants for exciton relaxations in the one-exciton manifold were already given in eq 50. Now, let us assume that the matrix $\underline{\underline{Q}}$ diagonalizes $\underline{\underline{K}}$ as

$$\underline{\underline{Q}}^{-1} \underline{\underline{K}} \underline{\underline{Q}} = \underline{\underline{\Lambda}} \quad (56)$$

where the diagonal elements of Λ , i.e., $\Lambda_{jj} = \lambda_j$, are the eigenvalues of the rate constant matrix \underline{K} . By using the Q matrix, eq 54 can be rewritten as

$$\tilde{G}(s) = \underline{Q}(sI + \underline{\Lambda})^{-1}\underline{Q}^{-1} \quad (57)$$

Thus, the conditional probability $G_{kj}(t)$ is found to be

$$G_{kj}(t) = \sum_l \underline{Q}_{kl} \underline{Q}_{lj}^{-1} e^{-\lambda_l t} \quad (58)$$

In this section, we showed that the state-to-state transition rate constants are directly proportional to the magnitude of the cross frequency fluctuation correlation. Once the rate constant matrix is determined, the conditional probabilities can be directly calculated by using eq 58.

C. 2D Photon Echo Spectra. Combining all the theoretical results, for a general N -coupled chromophore system we finally obtain an expression for the 2D photon echo spectrum written as a sum of diagonal and off-diagonal contributions,

$$\begin{aligned} \tilde{S}_{\text{echo}}(\Omega_1, T, \Omega_3) = & \sum_{j=1}^N P_j \tilde{S}_{jj}(\Omega_1 = \bar{\omega}_{e_g}, T, \Omega_3 = \bar{\omega}_{e_g}) \\ & + \sum_{i=1}^N \sum_{j \neq i}^N P_i G_{ii}(T) \tilde{S}_{ij}^{(1)}(\Omega_1 = \bar{\omega}_{e_g}, T, \Omega_3 = \bar{\omega}_{e_g}) \\ & - \sum_{j=1}^N \sum_{k=1}^{N(N-1)/2} P_j G_{jj}(T) \tilde{S}_{jk}^{(2)}(\Omega_1 = \bar{\omega}_{e_g}, T, \Omega_3 = \bar{\omega}_{f_{ke}}) \\ & + \sum_{i=1}^N \sum_{j \neq i}^N P_i G_{ji}(T) \tilde{S}_{ij}^{(1)}(\Omega_1 = \bar{\omega}_{e_g}, T, \Omega_3 = \bar{\omega}_{e_g}) \\ & - \sum_{i=1}^N \sum_{j \neq i}^N \sum_{k=1}^{N(N-1)/2} P_i G_{ji}(T) \tilde{S}_{i-jk}^{(2)}(\Omega_1 = \bar{\omega}_{e_g}, T, \Omega_3 = \bar{\omega}_{f_{ke}}) \quad (59) \end{aligned}$$

The first summation term gives the diagonal peaks of both the R_2 and R_3 pathways when $e_i = e_j$ contribute to them. The second summation term in eq 59 describes the line shapes of off-diagonal cross-peaks at $(\Omega_1 = \bar{\omega}_{e_g}, \Omega_3 = \bar{\omega}_{e_g})$ originating from the R_3 pathways with $e_i \neq e_j$. Here, the superscript “(1)” on \tilde{S} emphasizes that it involves transitions between the ground and one-exciton states. Although R_2 pathways with $e_i \neq e_j$ exist, their contributions are small as their oscillations during the second delay time, $\exp(\pm i\bar{\omega}_{e_g} t_2)$, destructively interfere with one another when spectrally broad femtosecond pulses are used. For this reason, we only consider the diagonal contributions ($e_i = e_j$) from the R_2 pathways. The third summation term is associated with R_1^* pathways, where the transitions from a one-exciton state to a two-exciton state are involved. Note that superscript “(2)” is used to emphasize that it involves transitions to two-exciton states. Again, only R_1^* pathways for $e_i = e_j$ are considered. It should be emphasized that the overall magnitude of the third term (R_1^*) is negative so its contributions will destructively interfere with the first two terms. The first three terms in eq 59 contribute when the initially created one-exciton state population evolves in time T without undergoing exciton transport to the other one-exciton states. Therefore, these three terms are multiplied by the survival probability function, $G_{jj}(T)$. The fourth and fifth terms account for population transfer from a one-exciton state to another one-exciton state and its transport probability is described by the conditional probability function, $G_{ji}(T)$.

By using the results in section IV, we find that the three components in eq 59 are

$$\begin{aligned} \tilde{S}_{jj}(\Omega_1 = \bar{\omega}_{e_g}, T, \Omega_3 = \bar{\omega}_{e_g}) = & \frac{2\pi \langle \mu_{e_j}^4 \rangle}{\sqrt{\langle \delta \Omega_j^2 \rangle^2 (1 - a^2(T)/C_0^2)}} \\ & \times \exp\{-X_j^2(\bar{\omega}_{e_g})\} [\exp\{-Y_{jj}^2(\bar{\omega}_{e_g}, \bar{\omega}_{e_g})\} + G_{jj}(T) \\ & \times \exp\{-Y_{jj}^2(\bar{\omega}_{e_g} - 2\langle \delta \Omega_j^2 \rangle \sigma(T)/C_0, \bar{\omega}_{e_g})\}] \\ & \times \tilde{S}_{ij}^{(1)}(\Omega_1 = \bar{\omega}_{e_g}, T, \Omega_3 = \bar{\omega}_{e_g}) \\ = & \frac{2\pi \langle \mu_{e_i}^2 \mu_{e_j}^2 \rangle}{\sqrt{\langle \delta \Omega_i^2 \rangle \langle \delta \Omega_j^2 \rangle - \langle \delta \Omega_i \delta \Omega_j \rangle^2 a^2(T)/C_0^2}} \\ & \exp\{-X_i^2(\bar{\omega}_{e_g})\} \exp\{-Z_{ij}^2(\bar{\omega}_{e_g}, \bar{\omega}_{e_g})\} \\ & \times \tilde{S}_{jk}^{(2)}(\Omega_1 = \bar{\omega}_{e_g}, T, \Omega_3 = \bar{\omega}_{f_{ke}}) \\ = & \frac{2\pi \langle \mu_{e_i} \mu_{e_{f_k}} \mu_{e_j} \rangle}{\sqrt{\delta_j^2 \Delta_{jk}^2 - H_{jk}^2(T)}} \exp\{-X_j^2(\bar{\omega}_{e_g})\} \\ & \times \exp\{-\Lambda_{jk}^2(\bar{\omega}_{f_{ke}} - Q_{jk}(T), \bar{\omega}_{e_g})\} \quad (60) \end{aligned}$$

where the two remaining 2D spectral functions, $\tilde{S}_{ij}^{(1)}(\Omega_1 = \bar{\omega}_{e_g}, T, \Omega_3 = \bar{\omega}_{e_g})$ and $\tilde{S}_{i-jk}^{(2)}(\Omega_1 = \bar{\omega}_{e_g}, T, \Omega_3 = \bar{\omega}_{f_{ke}})$, in eq 59 and the auxiliary functions used above are provided in Supporting Information 3.

Note that linear spectroscopy measures the dipole strength for each exciton, whereas the cross-peaks in 2D spectroscopy, as shown in the equation above, access the dipole strength cross-correlation function between two different excitons, $\langle \mu_{e_i}^2 \mu_{e_j}^2 \rangle$.

Once the one- and two-exciton eigenvectors are determined from the constructed exciton Hamiltonian matrices, which are critically dependent on the specific complex under investigation, the time-evolved 2D photon echo spectra can be numerically calculated using the above equations.

VI. FMO Antenna Complex

Recently, time-resolved two-dimensional electronic spectra of the FMO pigment-protein complex from the green sulfur bacterium *Chlorobium tepidum* were obtained by performing heterodyne-detected three-pulse photon echo spectroscopy.²¹ The FMO protein was the first photosynthetic protein to be crystallized to atomic resolution (Figure 2).^{55–60} Although the FMO complex consists of a trimer of 21 bacteriochlorophyll *a* molecules (BChls), it has been shown that the optical spectrum of the FMO complex is mainly determined by the interactions within a single subunit.^{61–63}

The electronic structure of the FMO complex has been studied extensively, and the advent of 2D spectroscopy allows stringent testing of the validity of the different models for the complex. Vulto et al.^{64,65} obtained electronic coupling constants J_{mn} by considering the dipole-dipole interaction between individual pigments and determined the site energies by fitting the absorption, circular dichroism, linear dichroism, and triplet-singlet spectra. In this paper we obtain the excitonic energies from the linear absorption and 2D electronic spectra and use the coupling constants obtained by Vulto et al.^{64,65} with one exception: we reduce J_{56} to 40 cm⁻¹. The site energies can therefore be inferred from the excitonic energies and coupling constants. The resulting electronic Hamiltonian is presented in Table 1.

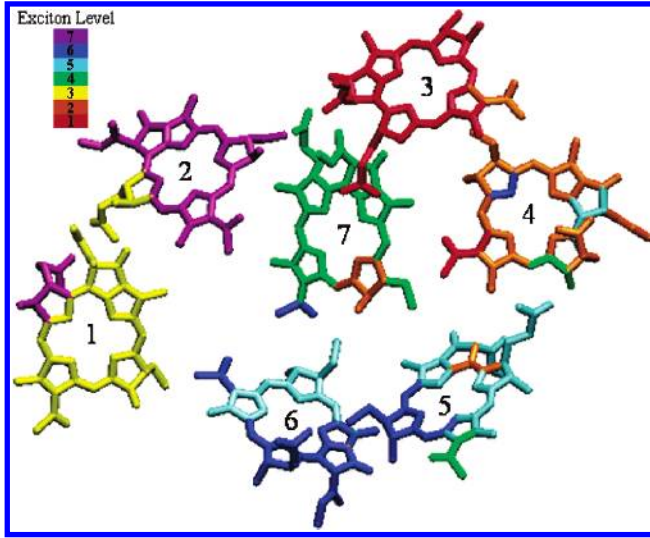


Figure 2. Pigment arrangement in a subunit of the FMO complex. The BChls are labeled following the original assignment by Fenna, Matthews, and Olson. Each BChl is colored according to its contribution to the one-exciton states. The exciton levels in the key are numbered in ascending energy order.

TABLE 1: One-Exciton Hamiltonian Matrix Elements for the FMO Complex (in cm^{-1})

	BChl 1	BChl 2	BChl 3	BChl 4	BChl 5	BChl 6	BChl 7
BChl 1	280	-106	8	-5	6	-8	-4
BChl 2	-106	420	28	6	2	13	1
BChl 3	8	28	0	-62	-1	-9	17
BChl 4	-5	6	-62	175	-70	-19	-57
BChl 5	6	2	-1	-70	320	40	-2
BChl 6	-8	13	-9	-19	40	360	32
BChl 7	-4	1	17	-57	-2	32	260

In this paper, we use modified Förster/Redfield theory,⁶⁶ eq 50, with a coupling cutoff of 30 cm^{-1} , to obtain the delocalized exciton state energies, exciton wave functions, and exciton relaxation rates. Therefore, only off-diagonal elements larger than 30 cm^{-1} in Table 1 were included in the diagonalization of the one-exciton Hamiltonian. The squares of the eigenvector elements of the seven exciton states are illustrated in Figure 2 and tabulated along with their corresponding dipole strengths, inverse participation ratios N_j , and fwhm (full width at half-maximum) in Table 2. Overall, the inverse participation ratios (IPR) are relatively small, suggesting that the exciton states are not strongly delocalized. Exciton 1 is mainly localized on BChl 3. Excitons 2 and 4 are delocalized on BChls 4 and 7, excitons 3 and 7 are both localized on BChls 1 and 2, and excitons 5 and 6 are on BChls 5 and 6. Therefore, we have $|e_3\rangle \approx 0.88 |1\rangle + 0.46 |2\rangle$, $|e_7\rangle \approx -0.46 |1\rangle + 0.87 |2\rangle$, $|e_5\rangle \approx -0.71 |5\rangle + 0.63 |6\rangle$, and $|e_6\rangle \approx 0.56 |5\rangle + 0.71 |6\rangle$.

To calculate the absorption spectrum we need to determine the spectral density and calculate the line shape functions. As discussed earlier in this paper, the electronic coupling reduces the line shape of each individual excitonic transition, so that the absorption spectrum should be calculated as

$$I(\omega) = \int_{-\infty}^{\infty} dt e^{i\omega t} \left\{ \sum_{j=1}^7 |\mu_e|_j^2 e^{-i\bar{\omega}_j t - g_j(t)} \right\} \quad (61)$$

where the line shape functions, $g_j(t)$, are defined as

$$g_j(t) = \int_0^t d\tau \int_0^\tau d\tau' \langle \delta\Omega_j(\tau') \delta\Omega_j(0) \rangle \approx \frac{1}{N_j} g_0(t) \quad (62)$$

Here, the line shape function of a single pigment in the limit of no coupling was denoted as $g_0(t)$ and is given by

$$g_0(t) \equiv \int_0^t d\tau \int_0^\tau d\tau' C(\tau') = -i\lambda t/\hbar + \int_0^\infty d\omega \rho(\omega) \coth\left[\frac{\hbar\omega}{2k_B T}\right] (1 - \cos \omega t) + i \int_0^\infty d\omega \rho(\omega) \sin \omega t \quad (63)$$

Note that the magnitude of the line shape function of the j th exciton transition is inversely proportional to the extent of delocalization, i.e., the inverse participation ratio N_j . We fit the experimentally measured absorption spectrum by using an Ohmic spectral density^{4,5,67,68} with $\omega_c = 50 \text{ cm}^{-1}$:

$$\omega^2 \rho(\omega) = (\lambda/\hbar) \frac{\omega}{\omega_c} \exp(-\omega/\omega_c) \quad (64)$$

We find that the solvent reorganization energy is 35 cm^{-1} and the static inhomogeneous width is 20 cm^{-1} . Thus, the fwhm of the line shape associated with the transition from the ground state to the j th exciton state is $2\sqrt{2\ln 2\{C_0 + 20^2\}N_j^{-1}} \text{ cm}^{-1}$. The experimental and simulated absorption spectra are shown in Figure 3. Except for the highest-energy peak at $12\,600 \text{ cm}^{-1}$, the overall line shape is in good agreement with experiment.

VII. Two-dimensional Spectroscopy of the FMO Complex

Experimental 2D Spectra. The Fenna–Matthews–Olson complex of *Chlorobium tepidum* was prepared in a buffer of 50 mM Tris and 10 mM sodium ascorbate as described elsewhere.⁵⁵ To resolve individual spectral features, we carried out the experiment at 77 K in a liquid nitrogen cryostat (Oxford). To prevent cracks in the low-temperature sample, we used a water–glycerol (35:65, v/v) mixture and plastic windows (thickness 0.3 mm) at 0.4 mm optical path length. The optical density peak value was 0.37.

Details of our 2D electronic spectroscopy setup have been provided elsewhere.¹⁵ Briefly, we use a home-built Ti:sapphire oscillator with a regenerative amplifier to generate 805 nm, 50 fs laser pulses at a repetition rate of 3 kHz. Three-pulse photon echo spectroscopy is performed using a phase-matched box geometry and heterodyne detection. We employ diffractive optics to achieve long-term phase stability and movable glass wedges to accurately delay the time between the first two pulses by τ with better than $\lambda/100$ precision. The population time T between the second and third pulse is controlled by a conventional delay stage external to the diffractive-optic setup. The signal is fully characterized in amplitude and phase by using spectral interferometry between the local oscillator and signal fields. Scattering effects are automatically reduced by recording and subtracting non-four-wave-mixing signals.

For any given population (waiting) time, T , the coherence time, τ , is scanned in 5 fs steps between ± 440 fs. Spectral interferograms are recorded with a 16-bit, 100×1340 -pixel, thermoelectrically cooled CCD camera (Princeton Instruments) and 0.3 m imaging spectrometer (Acton). These parameters lead to a spectral resolution of $7 \times 10^{-3} \text{ fs}^{-1}$ (37 cm^{-1}) for ω_τ and $3 \times 10^{-4} \text{ fs}^{-1}$ (1.6 cm^{-1}) for ω_r . The spot-size diameter at the sample position was $84 \mu\text{m}$ and the excitation energy 20 nJ per pulse. Experiments performed with 30% of the laser power led to essentially the same results. Data analysis by Fourier transformation yields the 2D traces of which we present the real parts in this paper, i.e., the absorptive contributions. The absolute phases of the 2D traces are obtained via the projection-

TABLE 2: Squares of the Eigenvector Elements, Inverse Participation Ratios, Dipole Strengths, and FWHM of Each One-exciton State in the FMO Complex^a

	exciton 1	exciton 2	exciton 3	exciton 4	exciton 5	exciton 6	exciton 7
BChl 1	0	0	0.7755	0	0	0	0.2245
BChl 2	0	0	0.2245	0	0	0	0.7755
BChl 3	0.8750	(-) 0.1137	0	0.0050	0.0048	0.0015	0
BChl 4	0.1149	0.5971	0	(-) 0.0981	(-) 0.1262	(-) 0.0637	0
BChl 5	0.0050	0.1096	0	(-) 0.1079	0.4529	0.3245	0
BChl 6	(-) 0.0002	(-) 0.0145	0	(-) 0.0295	(-) 0.4161	0.5397	0
BChl 7	0.0049	0.1650	0	0.7594	(-) 0.0000	0.0706	0
IPR	1.28	2.45	1.53	1.67	2.54	2.47	1.53
$ \mu_k ^2$	49	87	73	31	82	24	36
fwhm	141	102	129	123	100	102	129

^a The negative sign “(-)” indicates that the corresponding eigenvector element is negative. The unit of dipole strength is debye², and that of fwhm is cm⁻¹.

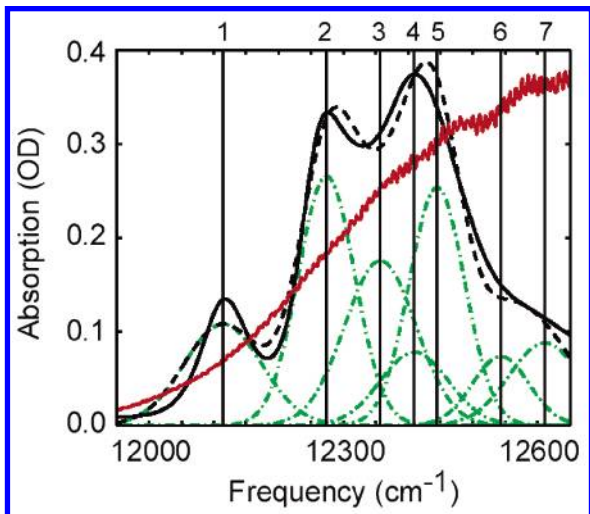


Figure 3. Experimental (solid black) and calculated (dashed black) linear absorption spectra for the FMO complex. The individual exciton contributions are also shown (dashed-dotted green). The laser spectrum used in the 2D experiments (red) covers all transition frequencies.

slice theorem and comparison with separately recorded spectrally resolved pump–probe data.^{29,31} Each 2D trace is the average of three separate scans. Following each series of 2D scans for different population times, we repeated the first scan in the same sample spot for comparison. The decrease in the magnitude of the 2D signal was less than 30% and the final trace gave qualitatively the same 2D results within the experimental noise.

Figure 4 shows the 2D spectrum for the FMO photosynthetic complex at population time $T = 0$ fs. The excitonic energies are indicated with solid lines. The 2D spectrum is asymmetric and we see several cross-peak features demonstrating the strong coupling between certain pigments. The lowest exciton state is easily discernible as the diagonal peak at $(\omega_t = \Omega_1, \omega_\tau = \Omega_1)$; hereafter labeled 1,1) and strong diagonal peaks are also observed for exciton positions 2 and 4, in accordance with the linear absorption spectrum (Figure 3). The mutual correlations of different excitons appear qualitatively as the magnitude of the corresponding cross-peaks. For example, we can deduce from Figure 4 that the BChl pigments that make up excitons 2 and 5 are coupled. The negative regions (dark blue, dashed contour lines) can be attributed to two-exciton contributions.

The time evolution of experimental 2D traces for population times up to 1 ps will be explained in detail and compared with simulations in section VII-D. The cross-peaks intensify over time, substantial exciton relaxation takes place giving rise to the “ \angle ”-shape of the main peak and the intense cross-peak formed between the lowest exciton state and the other exciton states. At 1 ps, the contributions arising from the different

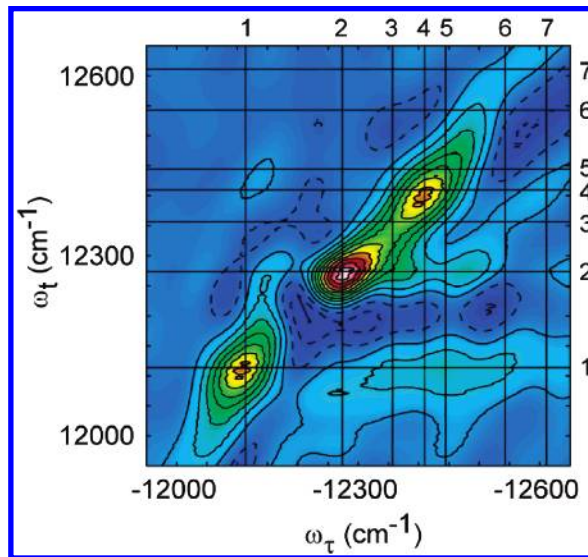


Figure 4. Experimentally measured 2D photon echo spectrum at $T = 0$. The positions of the calculated exciton states are marked on the figure.

exciton states are fairly well separated, making it possible to determine the different exciton energies.

B. Spatial Overlap between Exciton State Probability Densities and the Origin of Cross-Peaks. Since the one- and two-exciton Hamiltonians can be readily constructed by using parameters such as site energies and electronic coupling constants, with the above formalism we can now directly calculate the 2D spectra. However, we will first consider several interesting properties that affect the detailed 2D spectral patterns observed in the experiment. As discussed in section IV-E, the magnitudes of the fluctuating transition frequencies cross-correlation function of the j th and k th exciton states, $\langle \delta\Omega_j \delta\Omega_k \rangle$, is linearly proportional to the spatial overlap between the two exciton probability densities (see eqs 40 and 41). Within conventional Redfield theory, the exciton transfer rate between the j th and k th exciton states is also linearly proportional to $\langle \delta\Omega_j \delta\Omega_k \rangle$.⁶⁹ Thus, the magnitudes of the $\langle \delta\Omega_j \delta\Omega_k \rangle$ can be considered as measures of electronic couplings and exciton transfer rates. Note that the exciton transfer rate is also critically dependent on the amplitude of the spectral density at the frequency of the energy difference between the j th and k th exciton states. By tabulating the values of $\langle \delta\Omega_j \delta\Omega_k \rangle / C_0$ in Table 3 we observe interesting coupling patterns.

The probability density of the lowest-energy exciton state, which is localized on BChls 3 and 4, strongly overlaps with exciton 2. This is because exciton 2 is also delocalized over BChl 3 and BChl 4 (see Table 2). Since the excited states of BChls 3 and 4 contribute to both excitons 1 and 2, the transition frequency fluctuations of BChls 3 and 4 will simultaneously

TABLE 3. Relative (dimensionless) Magnitudes of the Transition Frequency Cross-correlation Function ($\langle\delta\Omega_j\delta\Omega_k\rangle/C_0$) for the One-exciton States of FMO

exciton	1	2	3	4	5	6	7
1	0	0.1695	0	0.0199	0.0210	0.0107	0
2	0.1695	0	0	0.1968	0.1316	0.0933	0
3	0	0	0	0	0	0	0.3482
4	0.0199	0.1968	0	0	0.0736	0.1108	0
5	0.0210	0.1316	0	0.0736	0	0.3796	0
6	0.0107	0.0933	0	0.1108	0.3796	0	0
7	0	0	0.3482	0	0	0	0

modulate the transition frequencies of excitons 1 and 2, making the cross-correlation magnitude $\langle\delta\Omega_1\delta\Omega_2\rangle$ as large as 0.17. Due to the intrinsic cross-correlation between $\delta\Omega_1(t)$ and $\delta\Omega_2(t)$, there could be a strong cross-peak at the position (1,2) (corresponding to $\omega_r = \Omega_1$, $\omega_\tau = \Omega_2$) even at very short times.

The transition frequency of exciton 2 is also strongly correlated with those of excitons 4 and 5. This phenomenon can be understood by examining the probability densities (Table 2, Figure 2). Note that exciton 2 is delocalized over BChls 4, 5, and 7 and that the probability densities of excitons 4 and 5 have sizable weights at BChls 4, 5, or 7. Therefore, site energy fluctuations induced by BChl bath interactions make the fluctuations of excitons 1, 4, and 5 in-phase with that of exciton 2.

The transition frequency of exciton 3 is solely correlated with that of exciton 7. Both excitons are formed as a result of the strong coupling between BChls 1 and 2 (see the Hamiltonian in Table 1). The large spatial overlap between the two excitons leads to the second largest value of $\langle\delta\Omega_j\delta\Omega_k\rangle$. The largest correlation occurs for excitons 5 and 6 which are largely localized on BChls 5 and 6. As we will see in the next section, the relaxation rate between excitons is roughly proportional to their spatial overlap. Hence, the large spatial overlap of these excitons greatly influences the overall population relaxation dynamics of FMO.

As discussed in detail above, the cross-correlations among fluctuating excitonic transition frequencies, $\langle\delta\Omega_j\delta\Omega_k\rangle$, are the electronic coupling effects. Similarly, the cross-peak amplitudes that are related to the orientationally averaged products of the squares of the transition dipole moments, $\langle\mu_{ej}^2\mu_{ek}^2\rangle$, become nonzero when the chromophores are electronically coupled. However, these two quantities are not directly related to each other, even though their physical origins are the same. One can understand the difference between them by examining eqs 26 and 40. $\langle\delta\Omega_j\delta\Omega_k\rangle$ is determined by the products of the squares of the eigenvector elements so that the electronic phase (sign of each eigenvector element) information is lost. On the other hand, the transition dipole between the ground and one-exciton states is given by a linear combination of transition dipoles of chromophores, and the weighting factors are the eigenvector elements. Consequently, the signs of eigenvector elements are crucial in this case. Therefore, there is no simple relationship between the cross-correlations among fluctuating excitonic transition frequencies and the cross-peak amplitudes, even though they are both nonzero only when the chromophores are electronically coupled to one another. Note that, if there is no electronic coupling, the EA and GB contributions will cancel, making the cross-peak disappear. The essence of the distinction between the two quantities is as follows: $\langle\delta\Omega_j\delta\Omega_k\rangle$ is a property of the system independent of any specific experiment. However, we observe the system via a specific four-wave mixing experiment, and this necessarily brings in the transition dipole moment factor $\langle\mu_{ej}^2\mu_{ek}^2\rangle$. From the PDB structure of FMO and the Hamiltonian in Table 1, we compute $\langle\mu_{ej}^2\mu_{ek}^2\rangle$ (Table 4). The largest values of $\langle\mu_{ej}^2\mu_{ek}^2\rangle$ occur between excitons (2,3),

TABLE 4: Relative (dimensionless) Magnitudes of the Orientationally Averaged Quantity, $\langle\mu_{ej}^2\mu_{ek}^2\rangle$

exciton	1	2	3	4	5	6	7
1	0	2.89	3.39	1.34	6.69	0.80	3.19
2	2.89	0	11.45	2.32	6.60	2.55	2.25
3	3.39	11.45	0	1.57	4.01	1.93	1.97
4	1.34	2.32	1.57	0	2.62	0.61	1.57
5	6.69	6.60	4.01	2.62	0	1.81	5.21
6	0.80	2.55	1.93	0.61	1.81	0	0.59
7	3.19	2.25	1.97	1.57	5.21	0.59	0

^a When the ground-state bleaching contribution is dominant, the cross-peak intensity is proportional to $\langle\mu_{ej}^2\mu_{ek}^2\rangle$.

TABLE 5: Exciton Relaxation Rates (in ps⁻¹) Calculated Using Modified Förster/Redfield Theory

exciton	1	2	3	4	5	6	7
1	0.12	-2.97	-0.12	-0.08	-0.03	0.00	0.00
2	-0.12	3.58	-0.28	-5.38	-1.60	-0.22	0.00
3	0.00	-0.07	0.46	-0.05	-0.17	-0.01	-1.60
4	0.00	-0.48	-0.02	6.60	-2.00	-2.46	0.00
5	0.00	-0.07	-0.03	-0.91	4.73	-5.73	-0.16
6	0.00	0.00	0.00	-0.18	-0.92	8.64	-0.68
7	0.00	0.00	-0.01	0.00	-0.01	-0.22	2.45

^a Rates faster than 1 ps⁻¹ are in bold.

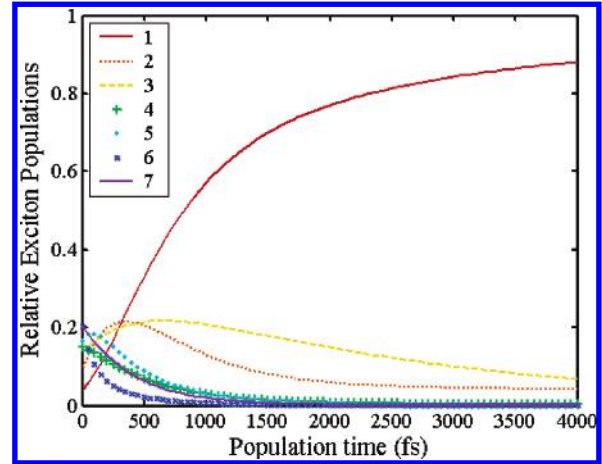


Figure 5. Time-evolution of the exciton state populations calculated using the spectral distribution of the laser intensity and the rate matrix in Table 5.

(1,5), and (2,5). The strong correlations within these pairs of excitons lead to the main cross-peaks observed (in the downhill positions) at $T = 0$ fs (Figure 4). The cross-peaks are not apparent in the uphill positions due to destructive interference with EA (see section VII-D).

The consequences of the distinction between $\langle\delta\Omega_j\delta\Omega_k\rangle$ and $\langle\mu_{ej}^2\mu_{ek}^2\rangle$ are important and become evident in the remainder of this paper; the former is related to the rate of energy transfer and line-broadening, the latter to the intensity of the cross-peak. This implies that rapid energy transfer can occur between two excitons; however, they may not form a cross-peak in the 2D spectrum at $T = 0$ fs. For example, excitons 3 and 7 have the largest spatial overlap, and we would expect direct energy relaxation from exciton 7 to 3, yet there is no discernible cross-peak at (3,7). Similarly, the cross-peak at (1,2) is small even though excitation of exciton 2 results in direct relaxation to exciton 1. In the remainder of this paper, we discuss the exciton relaxation dynamics within FMO and their contribution to the 2D spectra.

C. Exciton Transfer Rates: Master Equation Approach. Using the Hamiltonian in Table 1 and the Ohmic spectral density from section VI, we calculate the exciton relaxation rates using

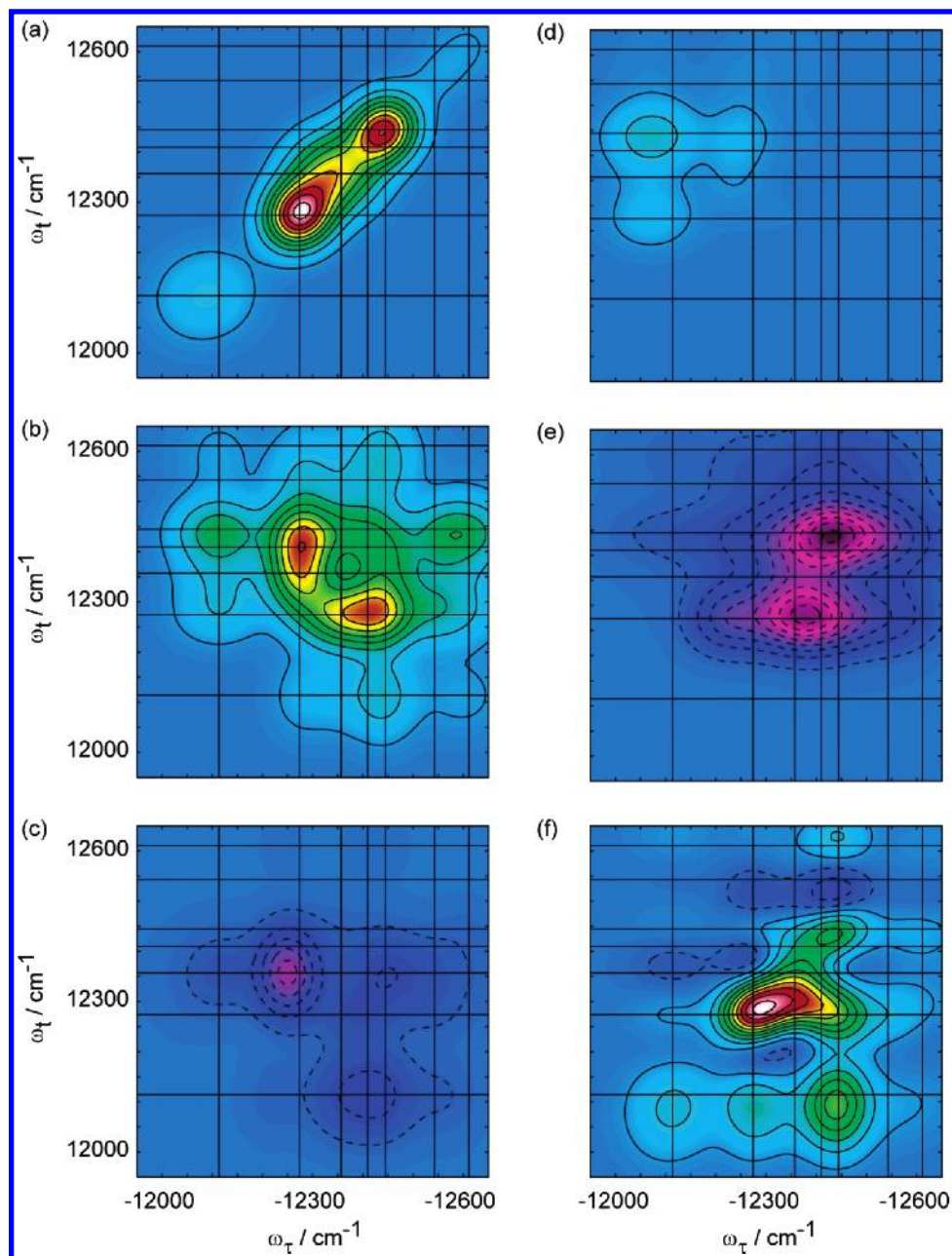


Figure 6. Components of the 2D signal at 1 ps. The individual contributions are all drawn on the same relative scale: (a) diagonal ground state bleach and stimulated emission, (b) off-diagonal ground state bleach and stimulated emission, (c) excited state absorption, when the initially created population states at $|e_j\rangle$ survive over T , (d) stimulated emission and (e) excited state absorption contributions when the initially created population state transfers to another one-exciton state during T . (f) The total signal (shown normalized) is obtained by summing over the individual terms.

modified Förster/Redfield theory with a coupling cutoff of 30 cm^{-1} (Table 5). Rates calculated using conventional Redfield theory are generally too slow when weakly coupled pigments are also present in the system. The rates calculated using modified Redfield theory with and without a Förster coupling cutoff are very similar, but the difference between these two theories actually lies in the nature of the exciton states. When we use modified Förster/Redfield theory, only pigment–pigment coupling strengths larger than 30 cm^{-1} are considered strong enough to change the nature of the excited state, and are included in the diagonalization of the Hamiltonian, and therefore the determination of the exciton energies. Coupling strengths weaker than 30 cm^{-1} are not included in the diagonalization of the Hamiltonian, but are used in the calculation of the rate matrix by invoking Förster theory. Therefore, even though the two rate matrices are similar, the corresponding Hamiltonians and wave

functions may not be, leading to different simulated absorption and 2D spectra. We found the absorption and 2D spectra obtained by using modified Förster/Redfield theory with a coupling cutoff of 30 cm^{-1} were in better agreement with experiment compared to the spectra obtained by using pure modified Redfield theory (corresponding to a cutoff of 0 cm^{-1}).

The rate matrix (Table 5) reveals patterns already observed in the spatial overlap of the excitons. Excitons 3 and 7 have a large spatial overlap, and hence excitation at exciton 7 relaxes directly to state 3. Due to the spatial isolation of BCHs 1 and 2, the lifetime of exciton 3 is quite long (as observed in pump–probe experiments⁶⁵) and relaxation from exciton 3 to exciton 1 or 2 occurs very slowly. Exciton level 6 results in direct decay to excitons 4 and 5; exciton 5 decays to exciton 4; exciton 4 decays to exciton 2, and exciton 2 decays to exciton 1. This

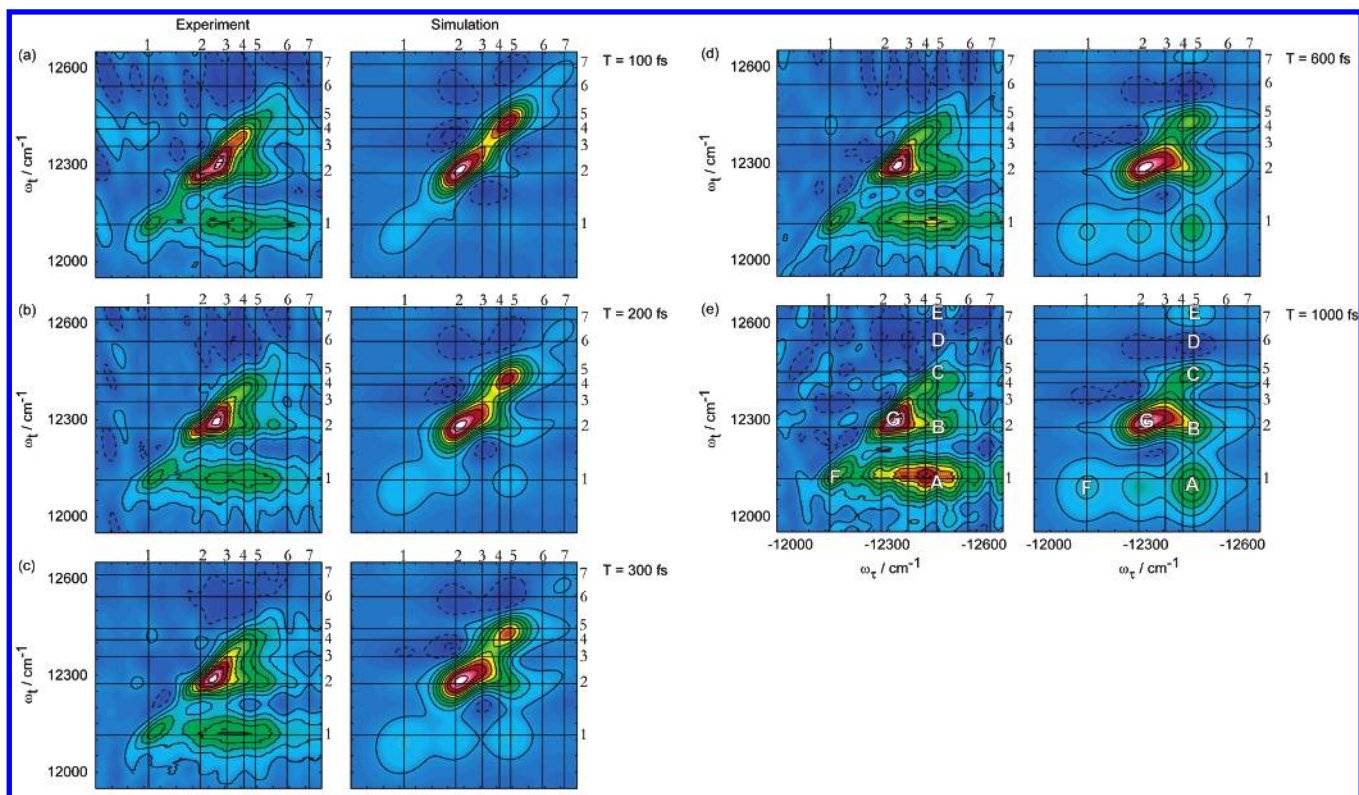


Figure 7. Experimentally measured (left) and numerically simulated (right) 2D spectra of FMO. The absorptive (real) part is shown for different population times at (a) $T = 0$ fs, (b) $T = 200$ fs, (c) $T = 300$ fs, (d) $T = 600$ fs, and (e) $T = 1000$ fs. Positive signals (“increased light”) are indicated by solid contour lines, negative signals (“decreased light”) by dashed lines. All traces have been normalized, the absolute signal decays with T .

leads to effectively two pathways: $7 \rightarrow 3 \rightarrow 1$ and $6 \rightarrow 5, 4 \rightarrow 2 \rightarrow 1$. The features observed in the 2D spectra are mostly due to the second pathway because it involves more pigments and these exciton states have large oscillator strengths.

If we estimate the initial populations by considering the spectral distribution of the laser intensity we can calculate the time evolution of the exciton state populations (Figure 5). Exciton 6 decays the fastest and is barely populated at 500 fs. Figure 5 clearly shows that excitons 2 and 3 are the intermediate receptors of energy. As exciton states 4–7 decay, the population of excitons 2 and 3 initially increases, and then decreases as the population relaxes further to exciton 1. Note that at time $T = 1000$ fs, only exciton states 1 and 3 are dominant. This observation is consistent with the transient pump–probe experimental findings by Vulto et al.^{62,65}

D. Simulated 2D Spectra, Comparisons, and Discussion.

Once the rate constants are calculated, we can directly calculate the time-evolution of the two-dimensional photon echo spectrum using eqs 59, 60, and 3S-1, 3S-2. Figure 6 shows the various contributions (a–e) to the total 2D spectrum (f) at a population time of 1000 fs. The contributions from pathways involving EA, (c) and (e), are negative and interfere with the other components of the 2D signal. The interference between these contributions makes it difficult to interpret 2D spectra without full analysis via simulation. As can be seen, the amplitudes of the various elements are of similar magnitude; therefore, the negative contributions cannot be neglected. The full 2D spectrum is obtained by summing these contributions. If there is no exciton migration process, the GB and SE contributions are symmetric in the 2D frequency domain. However, due to the asymmetry in the rate constant matrix, i.e., uphill transition rates < downhill transition rates, the entire 2D spectrum becomes asymmetric. Furthermore, the transitions from the one-exciton manifolds to

the two-exciton manifolds add an additional asymmetric component to the 2D spectrum. In the limit of zero electronic couplings, the EA contribution will cancel the off-diagonal GB+SE contribution to make all cross-peaks disappear, as expected. Consequently, the off-diagonal features of the 2D spectrum at $T = 0$ indicate that the quantum states involved in the optical excitation and subsequent relaxation of the FMO complex are spatially delocalized due to finite interchromophore couplings.

Figure 7 shows the experimental and simulated 2D spectra at varying population times. Overall, the 2D line shapes are qualitatively and quantitatively similar to experiment. The elongation of the diagonal peaks (representing the static inhomogeneity) is quite apparent, even at longer times and is reproduced well in our simulations. The absence of diagonal elongation of the cross-peaks is also simulated, suggesting that memory is not conserved upon excitation transfer. The amplitude and “L”-shape of the main peak is reproduced well at all population times, as is the rise in the amplitude of the cross-peaks, for example the cross-peak at (1,5) (labeled A in Figure 7e) and the cross-peak at (2,5) (labeled B). These cross-peaks are the most intense and are caused by relaxation from the 3rd, 4th, and 5th excitons to excitons 1 and 2 respectively (see also Table 4). We can quantitatively compare the theoretical and experimental results by calculating the amplitude ratios of the various peaks. For example, the amplitude ratio of diagonal peak C to diagonal peak G at $T = 1$ ps is measured to be 0.37, compared to the calculated value of 0.34. Similarly, the amplitude ratio of cross-peak B to diagonal peaks C and G at $T = 1$ ps is measured (and computed) to be 1.49 (1.45) and 0.55 (0.5), respectively. An uphill cross-peak at (7,5; E) is also observed in the experimental and simulated spectra at longer population times. Several negative features, for example at ω_c ,

$\sim 12550\text{ cm}^{-1}$, $\omega_{\tau} \sim 12300\text{--}12450$; D) are also reproduced in the simulations. Quantitatively, the calculated amplitude ratio of D to G at $T = 1\text{ ps}$ is roughly twice that of the experimental amplitude. However, if we compare the measured negative peak at (6,3) to the calculated negative peak at D, the amplitude ratios (with respect to peak G) are almost identical: -0.18 in the experimental spectrum vs. -0.19 in the theoretical spectrum. This suggests we calculated the amplitude of D correctly, but not the peak position.

There are also some discrepancies between the simulations and experiment. In the simulated spectra, the amplitude of the lowest-energy diagonal peak at (F) is approximately three times too weak at $T = 1\text{ ps}$, and at $T = 100\text{ fs}$ the third diagonal peak at 12450 cm^{-1} (C) is roughly twice as strong as the measured spectra. While the amplitude and position of the cross-peak at B matches that of the experimental data, the cross-peak amplitude ratio of A (1, 5) to G is calculated to be two-thirds too small: 0.48 compared to the observed value of 0.76 . In addition, cross-peak A is less elongated along ω_{τ} compared to experiment. One reason for this is the finite experimental frequency resolution (38 cm^{-1}) along ω_{τ} . There also appear to be more cross-peaks in the experimental data than in the simulations.

In summary, the experimental data are reasonably well reproduced by the simulations. This is very promising given the complexity of the physical system and the calculations. Because of the wealth of information that needs to be explained in 2D spectroscopy, such agreement gives strong evidence that the energy transport pathways and underlying mechanisms described above are correct. Our combined experimental and theoretical study shows that 2D time- and frequency-resolved electronic spectroscopy provides spatiotemporal information that is inaccessible through linear spectroscopy.

Providing a full quantitative analysis of all the features of the 2D spectra will provide a searching test for the state-of-the-art in electronic structure, molecular coupling, and quantum dynamical calculations. For example we know that the point dipole approximation is often inadequate in photosynthetic complexes,^{2,70} and that electronic coherence transfer has been neglected in our relaxation theory.^{71,72}

VIII. Summary and a Few Concluding Remarks

We have presented the necessary theory to calculate the full two-dimensional electronic spectra of any molecular aggregate containing coupled pigments. We have shown that the cross-peaks in 2D electronic spectra are proportional to the dipole strength cross-correlation function between two different excitons, $\langle \mu_{e_i}^2 \mu_{e_j}^2 \rangle$, a quantity that cannot be obtained from linear spectroscopy. The spatial overlap between exciton state probability densities also strongly influences the amplitude of the electronic cross-peaks. We apply this theory to simulate 2D electronic spectra of the Fenna–Matthews–Olson (FMO) photosynthetic complex²¹ and obtain spectra in excellent agreement with experimental results. Thereby we arrive at a picture for how the initially absorbed photon energy is transported, with two separate energy relaxation pathways.

In more general terms, this allows us to follow electronic energy transfer through space (on a molecular-scale resolution) and time (on a femtosecond scale). Furthermore, the underlying transport mechanisms (electronic couplings and excitonic wave function overlaps) can be deduced. This gives us detailed insight into the design principles of photosynthetic light harvesting. Applications to many other photoactive systems are possible.

The high information content of 2D (electronic) spectroscopy in general provides the means to determine Hamiltonians of

molecules and molecular complexes on a very detailed level. Potential future developments include high-quality electronic structure calculations to obtain accurate Coulombic coupling in such confined geometries,^{69,73} allowing to test the ability of quantum chemical methods to predict the electronic structure of molecular complexes, and of quantum dynamical theories to accurately describe the evolution of excited states. By combination with experiment such as shown here, we can arrive at a detailed understanding of the excited-state dynamics of complex (coupled) systems.

Acknowledgment. This work was supported by the CRIP (KOSEF, Korea) and by the Director, Office of Science, Office of Basic Energy Sciences, Chemical Sciences Division, of the U.S. Department of Energy under Contract No. DE-AC03-76SF00098. T.B. thanks the German Science Foundation (DFG) for an Emmy Noether fellowship, and J.S. thanks the German Academic Exchange Service (DAAD) for a postdoctoral fellowship. The apparatus for 2D spectroscopy was constructed by Igor Stiopkin and T.B. We thank Y.-Z. Ma, L. Valkunas, and M. Yang for helpful discussions and R. E. Blankenship for providing the FMO sample.

Supporting Information Available: Auxiliary functions and expansion coefficients. This material is available free of charge via the Internet at <http://pubs.acs.org>.

References and Notes

- (1) van Amerongen, H.; Valkunas, L.; van Grondelle, R. *Photosynthetic Excitons*; World Scientific: Singapore, 2000.
- (2) Fleming, G. R.; Scholes, G. D. *Nature* **2004**, *431*, 256.
- (3) Sumi, H. *J. Phys. Chem. B* **1999**, *103*, 252.
- (4) Fleming, G. R.; Cho, M. H. *Annu. Rev. Phys. Chem.* **1996**, *47*, 109.
- (5) de Boeij, W. P.; Pshenichnikov, M. S.; Wiersma, D. A. *Annu. Rev. Phys. Chem.* **1998**, *49*, 99.
- (6) Mukamel, S. *Annu. Rev. Phys. Chem.* **2000**, *51*, 691.
- (7) Jonas, D. M. *Annu. Rev. Phys. Chem.* **2003**, *54*, 425.
- (8) Hybl, J. D.; Albrecht, A. W.; Gallagher Faeder, S. M.; Jonas, D. M. *Chem. Phys. Lett.* **1998**, *297*, 307.
- (9) Lepetit, L.; Joffre, M. *Opt. Lett.* **1996**, *21*, 564.
- (10) Hybl, J. D.; Ferro, A. A.; Jonas, D. M. *J. Chem. Phys.* **2001**, *115*, 6606.
- (11) Fleming, G. R.; Yang, M.; Agarwal, R.; Prall, B. S.; Kaufman, L. J.; Neuwahl, F. V. R. *Bull. Korean Chem. Soc.* **2003**, *24*, 1081.
- (12) Cina, J. A.; Kilin, D. S.; Humble, T. S. *J. Chem. Phys.* **2003**, *118*, 46.
- (13) Prall, B. S.; Parkinson, D. Y.; Yang, M.; Ishikawa, N.; Fleming, G. R. *J. Chem. Phys.* **2004**, *120*, 2537.
- (14) Brixner, T.; Mancal, T.; Stiopkin, I.; Fleming, G. R. *J. Chem. Phys.* **2004**, *121*, 4221.
- (15) Brixner, T.; Stiopkin, I. V.; Fleming, G. R. *Opt. Lett.* **2004**, *29*, 884.
- (16) Cowan, M. L.; Ogilvie, J. P.; Miller, R. J. D. *Chem. Phys. Lett.* **2004**, *386*, 184.
- (17) Yang, M.; Fleming, G. R. *J. Chem. Phys.* **1999**, *110*, 2983.
- (18) Van Dao, L.; Lincoln, C.; Lowe, M.; Hannaford, P. *J. Chem. Phys.* **2004**, *120*, 8434.
- (19) Stiopkin, I.; Brixner, T.; Fleming, G. R.: Two-dimensional optical heterodyne spectroscopy of molecular complexes. In *Ultrafast Phenomena XIV*; Kobayashi, T., Okada, T., Kobayashi, T., Nelson, K. A., de Silvestri, S. Eds.; Springer Series in Chemical Physics; Springer: Berlin, **2005**; Vol. 79, pp. 554–556.
- (20) Stiopkin, I. *Resonant Heterodyne Two-Dimensional Optical Spectroscopy*; Columbia University: New York, 2005.
- (21) Brixner, T.; Stenger, J.; Vaswani, H. M.; Cho, M.; Blankenship, R. E.; Fleming, G. R. *Nature* **2005**, *434*, 625.
- (22) Cho, M. *Phys. Chem. Commun.* **2002**, *5*, 40.
- (23) Cho, M. *J. Chem. Phys.* **2001**, *115*, 4424.
- (24) Mukamel, S. *Principles of Nonlinear Optical Spectroscopy*; Oxford University Press: New York, 1995.
- (25) Hamm, P.; Lim, M.; DeGrado, W. F.; Hochstrasser, R. M. *Proc. Natl. Acad. Sci. U.S.A.* **1999**, *96*, 2036.
- (26) Asplund, M. C.; Zanni, M. T.; Hochstrasser, R. M. *Proc. Natl. Acad. Sci. U.S.A.* **2000**, *97*, 8219.

- (27) Golonzka, O.; Khalil, M.; Demirdoven, N.; Tokmakoff, A. *Phys. Rev. Lett.* **2001**, *86*, 2154.
- (28) Ge, N. H.; Zanni, M. T.; Hochstrasser, R. M. *J. Phys. Chem. A* **2002**, *106*, 962.
- (29) Fang, C.; Wang, J.; Kim, Y. S.; Charnley, A. K.; Barber-Armstrong, W.; Smith, A. B.; Decatur, S. M.; Hochstrasser, R. M. *J. Phys. Chem. B* **2004**, *108*, 10415.
- (30) Chung, H. S.; Khalil, M.; Tokmakoff, A. *J. Phys. Chem. B* **2004**, *108*, 15332.
- (31) McClain, B. L.; Finkelstein, I. J.; Fayer, M. D. *Chem. Phys. Lett.* **2004**, *392*, 324.
- (32) Demirdoven, N.; Cheatum, C. M.; Chung, H. S.; Khalil, M.; Knoester, J.; Tokmakoff, A. *J. Am. Chem. Soc.* **2004**, *126*, 7981.
- (33) Khalil, M.; Demirdoven, N.; Tokmakoff, A. *J. Chem. Phys.* **2004**, *121*, 362.
- (34) Krummel, A. T.; Mukherjee, P.; Zanni, M. T. *J. Phys. Chem. B* **2003**, *107*, 9165.
- (35) Wright, J. C. *Int. Rev. Phys. Chem.* **2002**, *21*, 185.
- (36) Woutersen, S.; Hamm, P. *J. Phys. Condens. Matter* **2002**, *14*, R1035.
- (37) Khalil, M.; Demirdoven, N.; Tokmakoff, A. *J. Phys. Chem. A* **2003**, *107*, 5258.
- (38) Cho, M.; Yu, J.-Y.; Joo, T.; Nagasawa, Y.; Passino, S. A.; Fleming, G. R. *J. Phys. Chem.* **1996**, *100*, 11944.
- (39) de Boeij, W. P.; Pshenichnikov, M. S.; Wiersma, D. A. *Chem. Phys.* **1998**, *233*, 287.
- (40) Everitt, K. F.; Geva, E.; Skinner, J. L. *J. Chem. Phys.* **2001**, *114*, 1326.
- (41) Kwac, K.; Cho, M. *J. Phys. Chem. A* **2003**, *107*, 5903.
- (42) Joo, T.; Jia, Y.; Yu, J.-Y.; Lang, M. J.; Fleming, G. R. *J. Chem. Phys.* **1996**, *104*, 6089.
- (43) de Boeij, W. P.; Pshenichnikov, M. S.; Wiersma, D. A. *J. Phys. Chem.* **1996**, *100*, 11806.
- (44) Fayer, M. D. *Annu. Rev. Phys. Chem.* **2001**, *52*, 315.
- (45) Zhang, W. M.; Meier, T.; Chernyak, V.; Mukamel, S. *J. Chem. Phys.* **1998**, *108*, 7763.
- (46) Zhang, W. M.; Meier, T.; Chernyak, V.; Mukamel, S. *Philos. Trans. R. Soc. London, Ser. A* **1998**, *356*, 405.
- (47) Fidler, H.; Knoester, J.; Wiersma, D. A. *J. Chem. Phys.* **1991**, *95*, 7880.
- (48) Ohta, K.; Yang, M.; Fleming, G. R. *J. Chem. Phys.* **2001**, *115*, 7609.
- (49) Kobayashi, T. *J-aggregates*; World Scientific: Singapore, 1996.
- (50) Redfield, A. G. *Adv. Magn. Reson.* **1965**, *1*, 1.
- (51) Yang, M.; Fleming, G. R. *Chem. Phys.* **2002**, *275*, 353.
- (52) Soules, T. F.; Duke, C. D. *Phys. Rev. B* **1971**, *3*, 262.
- (53) Rachovsky, S.; Silbey, R. *Mol. Phys.* **1973**, *25*, 61.
- (54) Kenkre, V. M.; Knox, R. S. *Phys. Rev. Lett.* **1974**, *33*, 803.
- (55) Li, Y. F.; Zhou, W. L.; Blankenship, R. E.; Allen, J. P. *J. Mol. Biol.* **1997**, *271*, 456.
- (56) Olson, J. M. Bacteriochlorophyll *a*-proteins from green bacteria. In *The Photosynthetic Bacteria*; Clayton, R. K., Sistrom, W. R., Eds.; Plenum Press: New York, 1978; p 161.
- (57) Matthews, B. W.; Fenna, R. E. *Acc. Chem. Res.* **1980**, *13*, 309.
- (58) Matthews, B. W.; Fenna, R. E.; Bolognesi, M. C.; Schmid, M. F.; Olson, J. M. *J. Mol. Biol.* **1979**, *131*, 259.
- (59) Fenna, R. E.; Matthews, B. W. *Nature* **1975**, *258*, 573.
- (60) Tronrud, D. E.; Schmid, M. F.; Matthews, B. W. *J. Mol. Biol.* **1986**, *188*, 443.
- (61) Louwe, R. J. W.; Vrieze, T.; Hoff, A. J.; Aartsma, T. J. *J. Phys. Chem. B* **1997**, *101*, 11280.
- (62) Vulto, S. I. E.; De Baat, M. A.; Neerken, S.; Nowak, F. R.; van Amerongen, H.; Ames, J.; Aartsma, T. J. *J. Phys. Chem. B* **1998**, *102*, 10630.
- (63) Renger, T.; May, V.; Kühn, O. *Phys. Rep.* **2001**, *343*, 137.
- (64) Vulto, S. I. E.; de Baat, M. A.; Louwe, R. J. W.; Permentier, H. P.; Neef, T.; Miller, M.; van Amerongen, H.; Aartsma, T. J. *J. Phys. Chem. B* **1998**, *102*, 9577.
- (65) Vulto, S. I. E.; de Baat, M. A.; Neerken, S.; Nowak, F. R.; van Amerongen, H.; Ames, J.; Aartsma, T. J. *J. Phys. Chem. B* **1999**, *103*, 8153.
- (66) Yang, M.; Damjanovic, A.; Vaswani, H. M.; Fleming, G. R. *Biophys. J.* **2003**, *85*, 140.
- (67) Cho, M.; Fleming, G. R. *J. Chem. Phys.* **1993**, *98*, 2848.
- (68) Vohringer, P.; Arnett, D. C.; Westervelt, R. A.; Feldstein, M. J.; Scherer, N. F. *J. Chem. Phys.* **1995**, *102*, 4027.
- (69) Kühn, O.; Sundstrom, V. *J. Chem. Phys.* **1997**, *107*, 4154.
- (70) Krueger, B. P.; Scholes, G. D.; Fleming, G. R. *J. Phys. Chem. B* **1998**, *102*, 5378.
- (71) Jean, J. M.; Friesner, R. A.; Fleming, G. R. *J. Chem. Phys.* **1992**, *96*, 5827.
- (72) Pislakov, A. V.; Gelin, M. F.; Domcke, W. *J. Phys. Chem. A* **2003**, *107*, 2657.
- (73) Hsu, C.-P.; Walla, P. J.; Head-Gordon, M.; Fleming, G. R. *J. Phys. Chem. B* **2001**, *105*, 11016.